Optimized CRISPR Perturbation Illuminates the Functions of RNA Modification Proteins

Ge Wei[1,#], Zhengyu Jing[1,#], Weikai Wang[2], Tian Chi[1,3]

[1]School of Life Science and Technology,
ShanghaiTech University, Shanghai 201210, China

[2]BGI Research, Shenzhen 518083, China

# Equal contributions

[3]Correspondence
Tian Chi
School of Life Science and Technology,
ShanghaiTech University,
393 Middle Huaxia Road, Pudong, 201210 Shanghai, China
chitian@shanghaitech.edu.cn

Abstract

A new frontier in functional genomics is to construct “Perturbation Atlas” that systematically profiles the effects of perturbation of all the mammalian genes across various cell types in health and disease. To this end, we have previously developed an *in situ* CRISPR screening platform in mice named iMAP, where Cas9 guides are “stored” in germline-transmitted transgenes but inducibly “released” (expressed) via Cre-mediated recombination. A major limitation of iMAP is a strong bias in guide representation following the recombination. We now report that this bias was effectively mitigated by eliminating a recombination hotspot at the transgene. We next profiled, across 46 tissues, the abundance of the guides targeting 71 (52%) genes encoding writers, readers and erasers of RNA modifications, revealing their context-specific functions. Furthermore, in a tumor model, we identified regulators of NK cell activation, which was validated in human NK cells, thus offering potential targets for improving cancer immunotherapy. Finally, a public database was established for accessing and analyzing iMAP data. Our study marks an important step toward the creation of the Perturbation Atlas.

Introduction

Decades after sequencing of the human genome, the context-specific functions of ~20000 protein-coding genes across hundreds of cell types in the human body in health and disease remain poorly defined. A pressing task in functional genomics research is to construct “Cell and Tissue Perturbation Atlas”, which involves systematic disruption of mammalian genome and deciphering of the resulting phenotypes at the cellular and tissue levels in a high-throughput manner in both human and animal models (Rood et al., 2024). Such an atlas can reveal causal relationship between genetic circuits and cellular phenotypes, thus complementing various observational atlases and omics studies, such as the Human Cell Atlas aimed at profiling gene expression patterns of all human cell types (Regev et al., 2017; Rood et al., 2024, 2022). Importantly, with increasing amounts of perturbation data, artificial intelligence and machine learning can be deployed to predict gene function, thus enabling a Perturbation Atlas to serve as a generative causal foundation model, which will greatly empower our understanding of human biology in health and disease (Rood et al., 2024).

Pooled CRISPR screening is a standard and powerful high-throughput method for exploring gene functions in cell culture (Joung et al., 2017) and in transplanted immune cells (Shi et al., 2023), but its direct application to the cells *in situ* in mice remains challenging due to

inefficient/uneven delivery of viral sgRNA libraries to target cells in their complex native environment(Braun et al., 2022; Chow and Chen, 2018; Fallon and Knouse, 2025; Kuhn et al., 2021). As a result, *in situ* screening has only been reported sporadically for a few solid organs (Jin et al., 2020; Keys and Knouse, 2022; Noguchi et al., 2024; Rogers et al., 2018, 2017; Santinha et al., 2023; Wertz et al., 2020; Zheng et al., 2024). To eradicate the delivery problem inherent in viral libraries, thus achieving systematic *in situ* perturbation of diverse tissues throughout the whole mice, we have combined CRISPR-Cas9 and Cre-LoxP technologies into a virus-free platform named inducible mosaic animal for perturbation (iMAP) (Cai and Winslow, 2022; Liu et al., 2022; Sun et al., 2023). iMAP uses a novel germline-transmitted transgene comprising 100 individually floxed gRNA-coding units ("guides") linked together in tandem (Fig. 1A). The array of guides is placed under the control of a modified U6 promoter with a LoxP variant (Lox71) embedded. In mice carrying the transgene and also ubiquitously expressing CreER and Cas9, treatment of mice with Tamoxifen (TAM), which activates Cre, would trigger recombination between Lox71 and one of the downstream LoxP sites preceding each guide (LoxTC9), leading to the expression of all the guides in the mice, but only one of them per cell, thus converting the mice into mosaic organisms ready for phenotypic characterization. iMAP is advantageous over conventional pooled *in situ* CRISPR screens, in that CRISPR perturbation can be readily induced via simple TAM administration, allowing parallel analyses of diverse cell types and tissues throughout the mice, with the mouse lines recurrently accessible as they can be maintained, propagated and shared just as conventional transgenic mice. Importantly, while pooled CRISPR screens typically use multiple gRNAs per target gene, the "one guide/target" design proves acceptable for iMAP, partly because the system's noise, as defined by random variations in non-targeting guide abundance, is low enough to allow robust detection of even subtle (1.5x) changes in guide representations (Liu et al., 2022). With a single iMAP mouse line, and using gRNA representation as the readout, we have rapidly constructed a miniature version of the mammalian perturbation atlas cataloguing the effects of perturbations of 90 genes across 39 organs/tissues/cells ("tissues" hereafter), which is hardly achievable using other tools. However, a major weakness of iMAP is that the recombination between Lox71 and the series of downstream LoxTC9 sites is biased toward the proximal (mainly the first 11) sites, leading to the underrepresentation of the distal guides at P0 in the post-recombination library, which necessitates the use of more cells in order to cover the distal guides (Figure 1A) (Liu et al., 2022). The bias in recombination thus compromises assay sensitivity, hampering the profiling of rare cells in the body.

90 All known types of RNA, including mRNA, tRNA and rRNA, are subject to dynamic chemical
91 modifications, which impacts RNA stability, subcellular localization and/or interactions with other
92 biomolecules (Cui et al., 2022; Qiu et al., 2023; Yi and Yang, 2023). The modifications are
93 deposited and removed by the "writers" and "erasers", respectively, whereas the "readers" bind
94 the modification marks and recruit effector machinery to alter cell functions, thus translating the
95 modification signals into functional outputs. RNA modification has emerged as a crucial
96 regulator of gene expression in health and disease, and is attracting increasing attention. The
97 latest version of the Modomics Database documents 335 RNA modifications in nature and 137
98 modification factors (writers, erasers and readers) in humans (https://genesilico.pl/modomics/)
99 (Cappannini et al., 2024). Traditionally, RNA modification is investigated mostly in cell culture.
100 KO mice have also been described for some of the modification factors (see further), but the KO
101 often proves lethal, precluding in-depth characterization. Thus, the roles of the modification
102 factors in mice, especially in various cell types in adults, remain largely unexplored.

103 In this study, we substantially improved the uniformity of guide representation in iMAP, which is
104 now comparable to that in conventional lentiviral sgRNA libraries used in pooled CRISPR
105 screens. We then interrogated the functions of 71 RNA modification factors across 46
106 organs/tissues/cell types ("tissues" hereafter) in adult mice. Furthermore, we combined iMAP
107 and a tumor model to identify candidate genes for potentiating tumor-killing function of NK cells,
108 which was subsequently validated in human NK cells. Finally, we describe a public iMAP
109 database.
110

111 Results

112 iMAP optimization via elimination of recombination hotspot

113 The Lox71-TC9 recombination in the first-generation iMAP transgene is biased toward g1-11,
114 indicating that the region encompassing g1-11, about 1.8 kb in length, is a recombination "hot
115 spot" (Figure 1A). We reasoned that its replacement with a 1.8-kb inert "stuffer" sequence
116 lacking LoxP sites might force TC71 to skip the "hotspot" to reach out to and rearrange with the
117 downstream TC9 sites, thus mitigating the bias in recombination. To test this, we constructed a
118 *91-guide* transgene with a 1.8-kb stuffer inserted between g0 and g1 (Figure 1B; see further for
119 guide composition). In the ensuing transgenic mice, the U6 promoter was active, unmethylated
120 and the *91-guide* array intact (Figure S1A-C). We profiled P0 guides in adult *91-guide; Cre* mice
121 at various levels of TAM-induced recombination, and compared the profiles with that in *100-*
122 *guide; Cre* mice at similar levels of recombination. There is indeed substantial improvement in

123 recombination uniformity in the *91-guide* array at all levels of recombination (Figure 2A), which
124 is more obvious if the guides are analyzed as groups (Figure 2B-C). Specifically, for the *100-*
125 *guide* array, the group comprising g1-10 was predominant, constituting up to 49-72% of the total
126 recombined P0 guides (yellow bar, Figure 2C top), contrary to the distal groups especially g41-
127 99 (1-5%; last six bars, Figure 2C top). In contrast, in *91-guide; Cre* mice, g1-10 dropped to 26-
128 34% while g41-90 rose to 6-15% (yellow vs last five bars, Figure 2C bottom), indicating marked
129 reduction in recombination bias.
130
131 iMAP sensitivity is limited by the least abundant P0 guide generated after recombination. We
132 found that in representative samples from the two mouse lines, each with 76% recombination (a
133 level typically achieved in our routine experiments), such guides constituted 0.1% and 0.35% of
134 the total P0 guides for the 100- and 91-guide transgene, respectively (Figure 2D). Thus, the
135 stuffer led to ~3.5x increase in sensitivity.

136 For iMAP analysis of rare cells, it can be challenging to isolate enough cells to cover all the
137 guides in the library, particularly the underrepresented guides. We thus used mathematical
138 modeling to explore the relationship between the numbers of cells sampled and the % of the
139 guides detected. We assume a detected guide is represented by at least 100 cells, a depth we
140 previously found sufficient for iMAP analysis, and we express cell number in relative terms, as
141 "fold over the total guide number in the array" (e.g., a value of 1 for the *100-guide* array means
142 100 cells sampled). For *100-guide*, the model predicts that the cell number must be at least
143 1000 times the guide number (namely 100,000 in absolute number) to detect 100% of the
144 guides, and the value drops to 75% and 50% when the cell number drops 2x and 4x,
145 respectively (Figure 2E, line 1). In contrast, for *91-guide*, cells only 300 times the guide number
146 suffice to cover all the guides, reinforcing the notion that the stuffer led to 3x increase in iMAP
147 sensitivity (Figure 3E, line 2). This sensitivity is still 3x lower than the theoretical limit achieved if
148 the recombination becomes absolutely even (Figure 3E, line 3), but already surpasses that of
149 conventional lentiviral library, in that full coverage of the viral library requires cells 500 times the
150 gRNA number, contrary to only 300 times for *91-guide* (Figure 3E, line 4). However, for partial
151 coverage, the viral library is slightly more sensitive (Figure 3E, line 4). Thus, on balance, the two
152 platforms perform similarly.

153 We conclude that the stuffer led to 3.5x increase in iMAP sensitivity, making it comparable to
154 that of the classic lentiviral sgRNA library.
155

156 **Overview of iMAP-91 phenotype**

157 As depicted in Figure 1B, the *91-guide* transgene features 78 guides targeting 71 RNA
158 modification genes (writers/erasers/readers), each gene targeted by one guide except that five
159 genes (*Alkbh3, Fto, Mettl3, Ythdc1, Ythdf1*) are each covered by several guides. The array also
160 carries a positive control targeting *Polr2a*, an essential gene whose perturbation causes cell
161 death, and nine non-targeting guides (negative control, NC) spiked into the array to control for
162 bias in recombination. We bred *91-guide; Ubc-CreER; CAG-Cas9* mice ("iMAP-91"), treated
163 them with TAM around D10 and analyzed guide representation in diverse tissues 3-4 months
164 thereafter in three females and three males. The mice were grossly normal except for atrophic
165 testes (Figure 3A). We have profiled P0 guides in 46 tissues sampled from six mice, yielding
166 4,002 data points (87 important guides x46 tissues) each averaged from at least two (mostly 4-6)
167 mice, the replicates being highly reproducible (Figure S2). Guide depletion events were
168 predominant, constituting 49% of the 4,002 data points using fold >= 2 as the threshold (black
169 lines) or 74% using gNC for comparison (green lines), contrary to only 0.1%–3% for the
170 enrichment and 23%–50% for the unaltered (Figure 3B). Note that the nine gNCs formed a
171 sharp peak, attesting to the low noise level of the system. We used simple bar graphs to display
172 the enriched guides (Figure 3C), and a heatmap to display depletion where the enrichment is
173 scored as "unaltered" to better visualize the depletion (Figure 3D).
174

175 **Guide enrichment in iMAP-91**

176 Enrichment was detected only for four guides (g63-*Rpusd4,* 15-*Trdmt1,* 48-*Snu13,* 62-*Trmu*) in
177 only three tissues, all the guides except g63 impacting cerebellum (Figure 3C). RPUSD4
178 pseudouridylates pre-mRNA, TRMU and TRDMT1 both modify tRNAs, while SNU13 binds U4
179 snRNA in the spliceosome. Little is known about their functions in mice, except that *Trmu* KO is
180 embryonic lethal (Wu et al., 2016) whereas *Trdmt1* KO less consequential (MGI:1274787),
181 echoing the conspicuous depletion of g62-*Trmu* but not g15-*Trdmt1*.
182

183 **Guide depletion in iMAP-91**

184 In the heatmap that displays guide depletion, the guides and tissues clustered into five (I–V) and
185 six (A–F) groups, respectively (Figure 3D). A caveat is that the guides were not pre-validated,
186 and so their activities could vary, thus affecting the clustering. However, the variation in the
187 cleavage rates of different targeting targets were quite moderate (60-80%) and not cluster-
188 specific as assayed *in vitro*, indicating that it did not have a (major) impact on clustering (Figure
189 3E). Furthermore, we previously observed four salient features in the iMAP-100 heatmap that

strongly support the biological relevance of clustering (Liu et al., 2022). Importantly, these features are all recapitulated in iMAP-91, as detailed below.

First, related guides tended to co-segregate. Thus, the eight gNC tightly co-segregated (gCluster I), as were guides targeting different essential subunits of the same protein complexes, including the following complexes: *Mettl3-Mettl14* (g53-56), *Iscu-Nfs1* (g83-84) , *Qtrt1-Qtr2* (g27-28) and to some extents *Trmt6-Trmt61a* (g77,69) and *Mettl1-Wdr4* (g65-76) (Figure 3D)(Johannsson et al., 2018; Li et al., 2023; Schaffrath and Leidel, 2017; Schmucker et al., 2011; Wang et al., 2016, 2021). Besides, the guides targeting four genes required for tRNA-U34 modifications (*Elp1*, *Elp3*, *Ctu1*, *Urm1*) tightly co-segregated (g42-45), although the guides targeting two other genes in the pathway (g16-*Alkbh8* and g73-*Trmt112*) did not (Figure 3F; see Discussion). Finally, different guides designed to inactivate the same genes, namely *Mettl3* (g53-55), *Ythdc1* (g66-67), *Ythdf1*(g17-18) and *Alkbh3* (g24,26,31), all (tightly) clustered (Figure S3A). On the other hand, guides predicted to impact the same genes but to different extents did not co-segregate, as in the case of *Fto* (g21, 41) and *Gon7* (g29, 85), albeit with the caveat that g85-*Gon7* additionally targets two unannotated genes related to *Gon7* (Figure S3B-C).

Second, relevant tissues tended to co-segregate just as relevant guides, including neural tissues (T2–9), skin-related tissues (T16-17, 20, 23, 25), intestine-related tissues (T26–29), lymphocyte subsets (T30–41), and male germ cell subsets (T42–46).

Third, guide depletion patterns in iMAP mice mirrored the phenotypes of conventional global single-gene KO mice. Thus, ablation of gCluster IV-V genes is all lethal (18/18), gClustre III mostly so (17/22) whereas gCluster I-II all viable except for two genes, *Mrm1* and *3* (2/12; Figure 3G). *Mrm1* and *Mrm3,* together with *Mrm2,* each encode essential mitochondrial rRNA methyltransferases whose KO each is lethal (Table S3), but g23-*Mrm1* and g14-*Mrm3* were only mildly depleted, contrary to g59-*Mrm2,* suggesting that *Mrm* family members all impact cell functions but only *Mrm2* markedly impact cell numbers.

Fourth, the genes generally required for cell survival in iMAP-91 were enriched with the ‘‘core essential genes’’ (CEGs) generally required for human tumor cell survival/proliferation (Hart et al., 2017). Specifically, of the 71 mouse genes targeted in iMAP-91, 12 were orthologous to human CEGs, all except three (34-*Trmt5*, 48-*Snu13*, 58-*Dimt1*) distributed among the last 21 mouse genes (73-87) in the heatmap (Figure 3D, pink text). Of note, g34-*Trmt5* was hardly depleted in most tissues, which was exceptional and of medical implications (see Discussion).

224 Collectively, these data highlight the robustness of the iMAP technology. We have begun to
225 mine the heatmap, as detailed below.

226 Tissue Cluster A: uniqueness of cerebellum

227 In this group of tissues (brain, heart, and eyeball), guide depletion was undetectable/weak
228 except for gCluster V (g76-87), which was clearly depleted in all tissues, suggesting that g76-87
229 had targeted CEGs. Guide alteration patterns were similar among various brain regions, but
230 comparison of cerebral cortex vs cerebellar central part (Tissue 05 vs 02) revealed multiple
231 guides with differential representations, which occurred due to different extents of depletion
232 (g*Gon7-1, Bud23, Mett16, Mepce*) or more interestingly to "qualitative" differences in guide
233 abundance (Figure 4A, top). Specifically, three guides (g48-*Snu13,* 15-*Trdmt1* and 62-*Trmu*)
234 were enriched in the cerebellum (Tissue 02-03) but no other brain region (Tissue 04-09; Figure
235 4A) or body tissue (Figure 3D), whereas g70-*Tprkb* was unaltered in the cerebellum but
236 generally depleted in other brain regions (Figure 4A) and body tissues (Figure 3D), exposing a
237 unique aspect of the cerebellum.
238

239 Tissue Cluster B: brown vs white fat

240 Brown fat (bFAT) burns calories and is located primarily in the interscapular region, whereas
241 white fat stores excess energy and is distributed widely, with perigonadal fat (pFAT) and
242 mesenteric fat (mFAT) among the major white adipose tissues. Three guides (g58, 59, 72) were
243 selectively depleted in pFAT and mFAT but not bFAT, suggesting that their target genes (*Dimt1*,
244 *Mrm2* and *Txn1*) selectively promote white adipocyte survival/proliferation/development without
245 impacting bFAT (Figure 4B).
246

247 Tissue Cluster D: small vs large intestine

248 Five guides were differentially represented in the epithelium of small vs large intestine, which
249 remarkably include the "tetra-guides" targeting tRNA-U34 modification (g42-*Elp1*, 43-*Elp3*, 44-
250 *Ctu1*, 45-*Urm1*; Figure 4C). Specifically, all the four guides were depleted clearly (2-4x) in the
251 epithelium of large intestine, whereas in the small intestine epithelium, the depletion was
252 marginal (~1.5x) and restricted to g*Ctu1/Urm1*, suggesting preferential requirement of tRNA-
253 U34 modification for the large intestine. Paradoxically, conditional *Elp3* KO in the intestinal
254 epithelium fails to produce overt phenotypes (Ladang et al., 2015). Perhaps the KO cells are
255 intrinsically defective, but the defect can only be exposed in the mosaic iMAP mice where the
256 KO cells tend to be surrounded by, and thus potentially in competition with, normal cells in the
257 same niche.

258

259 Tissue Cluster E: Regulators of T cell development and activation

260 gCluster III–V guides were generally depleted across various immune cells but occasionally to
261 different extents in pairs of closely related T cell subsets:

262

263 First, over a dozen guides were preferentially depleted in naïve CD4 T cells relative to Tregs,
264 with the tetra-guides that target tRNA-U34 modification among the top candidates (Figure 4D,
265 panel 1). The two T cell subsets develop from the same precursor (DP thymocytes), suggesting
266 that this lineage bifurcation is impacted by tRNA-U34 mofication.

267 Second, the tetra-guides targeting tRNA-U34 modification were also the top preferentially
268 depleted candidates in naïve relative to effector/memory(E/M) CD4 T cells (Figure 3D, panel 2).
269 Thus, tRNA-U34 modification seems a prominent repressor of both Treg development and CD4
270 T cell activation/differentiation. This function is specific, being absent from CD8 T cells; instead,
271 FTO, which erases N^6-methyladenosine (m^6A), emerged as a prominent repressor of CD8
272 differentiation into both E/M and central memory (CM) CD8 T cells (Figure 3D, panel 3-4). Of
273 note, multiple other guides were also enriched in CM relative to naïve CD8 cells (Figure 3D,
274 panel 4, red dots in the top plot), but these guides were severely depleted even in CM CD8 cells,
275 making their relative enrichment in CM CD8 cells less interesting (not shown).

276 Tissue cluster F: Spermatogonia vulnerability

277 Our previous analysis of iMAP-100 mice reveals striking vulnerability of spermatogonia, which is
278 recapitulated in iMAP-91:

279 First, spermatogonia were more vulnerable than their progeny (Figure 4E): out of the 79
280 targeting guides, only seven failed to impact spermatogenesis; the remaining 72 guides were
281 depleted at least 2x in spermatogonia, and no further change was seen in the progeny except
282 for g*Nsun2, Cmtr2* and *Elp1* (and to some extent g*Elp3*) whose depletion emerged in
283 spermatogonia and exacerbated in P/D (for g*Nsun2*) or RS (for g*Elp1/Elp3/Cmtr2*; Figure 4E). In
284 other words, 72 guides blocked spermatogonia survival/proliferation/renewal, but only three of
285 them additionally impacted its progeny. Of note, for the four guides targeting tRNA-U34
286 modification, depletion in spermatogonia was moderate (2-4x) for g*Elp1/3* but dramatic (24-38x)
287 for g*Urm1/Ctu1*, highlighting their functional dichotomy (see Discussion).

288

289 Second, spermatogonia were more vulnerable than somatic cells, in that gCluster II was
290 preferentially depleted in spermatogonia relative to somatic cells (Fig. 3D). In particular, four

291 guides (27-*Qtrt1*, 28-*Qtrt2*, 29-*Gon7-2* and 30-*Alkbh5*) were depleted marginally in somatic cells
292 but severely (6-27x) in the germline (Figure 4F). QTRT1 and QTRT2 form the heterodimeric
293 tRNA guanine transglycosylase (TGT) that catalyzes the base-exchange of a wobble guanine
294 (G34) with queuine (Q) in some tRNAs, with QTRT1 being the catalytic subunit(Sievers et al.,
295 2024). The co-depletion of both *Qtrt* guides strongly argues for the essential and selective role
296 of TGT in spermatogenesis. In an apparent conflict, a gene-trap cassette that eliminates a 48-aa
297 region required for QTRT1 catalytic activity fails to compromise spermatogenesis, perhaps
298 because the trapped allele still expresses the remaining 90% of QTRT1 (aa1–104 and 151-403)
299 (Rakovich et al., 2011). Regarding *Gon7*, it encodes a subunit of the KEOPS complex that
300 introduces tRNA N6-threonylcarbamoyladenosine (t6A) modification(Srinivasan et al., 2011).
301 g29-*Gon7-2* is predicted to eliminate the C-terminal 13 residues of GON7, thus revealing the
302 selective and essential role of this tail in spermatogonia (Figure S3C). Finally, *Alkbh5* encodes
303 an m6A eraser, and its global KO induces germ cell apoptosis and male sterility, but the mice
304 seem otherwise normal, which dovetails with the iMAP data, except that the apoptosis in the
305 global KO mice emerges at the pachytene stage whereas g30-*Alkbh5* was able to impact
306 spermatogonia (Zheng et al., 2013). This discrepancy may be reconcilable because in iMAP
307 mice, *Alkbh5*-deficient spermatogonia can be more vulnerable due to competition from normal
308 spermatogonia in the mosaic environment.
309
310 In summary, these data highlight the vulnerability of spermatogonia, which has medical
311 implications (see Discussion).

312 Uncovering potential therapeutic targets in a disease model: proof of concept

313 Finally, in a proof-of-principle study, we applied iMAP to a disease model to identify potential
314 targets for cancer immune therapy. We focused on natural killer (NK) cells, which are potent
315 tumor killers but prone to inhibition in tumor microenvironment (TME) (Coënon et al., 2024;
316 Maskalenko et al., 2022). Intense efforts are underway to re-activate NK in TME, typically by
317 blocking their negative regulators, but with limited success (Coënon et al., 2024; Maskalenko et
318 al., 2022). Our approach is to search for novel, more effective negative regulators of NK in TME.
319 Release of cytotoxic granules (marked by CD107a expression) and production of TNFα are
320 among the most important mechanisms of NK-mediated killing (González-Flores et al., 2014;
321 Park et al., n.d.). We thus sought to identify genes whose KO could elevate CD107a and TNFα
322 expression in NK cells within TME. To this end, we inoculated iMAP-91 mice with mouse colon
323 cancer MC38 cells, administered TAM to induce recombination, isolated and compared two
324 pairs of tumor-infiltrating NK subsets: CD107a^{hi} vs CD107a$^{low/-}$ and TNFα^{hi} vs TNFα$^{low/-}$ (Figure

325 5A). We found g66-*Ythdc1*-2 and g28-*Qtrt2* enriched in the CD107a ^{hi} relative to the CD107a$^{low/-}$
326 subset, with the same trend seen for g67-*Ythdc1*-1 but somehow not g14-*Qtrt1*, and g86-*Thg1l*
327 enriched in the TNFα^{hi} relative to the TNFα$^{low/-}$ subset (Figure 5B). Thus, *Ythdc1* (an m6A reader)
328 and *Thg1l* (involved in tRNA maturation) likely repressed NK degranulation and TNFα
329 expression in TME, respectively. To explore their therapeutic potential, we knocked out
330 *YTHDC1* and *THG1L* in human NK cells, co-cultured the KO cells with K562 human leukemia
331 cells for 6 hours, and analyzed both NK cells (for CD107a and TNFα expression) and K562 cells
332 (for lysis; Figure 5C). *YTHDC1* KO indeed substantially enhanced NK degranulation, with 3x
333 more cells expressing CD107a, but failed to boost K562 killing perhaps due to some
334 undesirable pleotropic effects of the KO (Figure 5D). On the other hand, *THG1L* KO enriched
335 TNFα in the culture media moderately (from 337 to 481 pg/ml), which was indeed concomitant
336 with increased K562 killing (from 39 to 65%; Figure 5E). *THG1L* KO did not enhance
337 degranulation as predicted, but unexpectedly, it failed to increase intracellular TNFα (Figure
338 S4A-B). After synthesis in the cytoplasm, TNFα is translocated to the plasma membrane and
339 subsequently released via cleavage by a protease. Perhaps in human NK cells *in vitro*, *THG1L*
340 KO increased TNFα production but also its release, thus canceling the increase in cellular TNFα
341 pool observed in iMAP-91 mice; the subtle discrepancy between the two systems might reflect
342 differences in the species (human vs mouse) and/or assay conditions (*in vitro* vs *in vivo*).
343 Finally, *THG1L* KO did not enhance perforin/granzyme B expression, reinforcing the role of
344 TNFα in increased killing (Figure S4C).
345
346 We conclude that iMAP is applicable to disease models for discovering potential drug targets.
347
348 iMAP website
349 We have constructed a public database for browsing, searching and analyzing iMAP data
350 (http://49.235.152.12/; Figure S5A). Four key modules are featured: “Heatmap”, which displays
351 interactive *Guide x Tissue* atlases (Figure S5B); “Gene Search”, which enables query for the
352 abundance of guides of interest across tissues (Figure S5C); “Network”, which presents an
353 interactive network of the guides surrounding a guide of interest, with relevant information
354 indicated, such as fold-changes of the guides, the number of tissues impacted by a guide, the
355 distances among the guides and the total number of guides connected with a particular guide
356 (Figure S5D); and “Tissue comparison”, which identifies the guides differentially represented
357 between a pair of selected tissues (Figure S5E). Future efforts should culminate in the creation
358 of the panoramic Perturbation Atlas covering all the genes across all the cell types at tissue and

359 single-cell levels.

360

361 ## Discussion

362 ### iMAP outperformed pooled *in situ* CRISPR screening

363 Genome-scale *in situ* CRISPR screening for essential genes using pooled lentiviral sgRNA
364 libraries have been applied to the mouse brain and liver, offering the opportunity to compare its
365 performance with that of iMAP. The pooled CRISPR screens uncovered 668 neuronal essential
366 genes (NEGs) and 661 hepatic essential genes (HEGs)(Keys and Knouse, 2022; Wertz et al.,
367 2020). Only one of the 668 NEGs was shared in iMAP-91, where the gene (*Thg1l*) was scored
368 as a CEG, with its guide severely and widely depleted in diverse tissues including the brain
369 (g86-*Thg1l* in gCluster V; Figure 3D). However, there were 11 other CEGS in iMAP-91, none of
370 them captured by the brain screen. The brain screen similarly hit only one of 12 CEGs identified
371 by iMAP-100, as reported before (Liu et al., 2022). Thus, between iMAP-91 and iMAP-100, a
372 total of 24 CEGs were identified, whose KO was lethal to the brain (and other tissues). However,
373 the lentiviral brain screen recovered only 8% (2/24) of these CEGs. The hepatic screen is
374 relatively more effective, recovering 50% (12/24) of the 24 CEGs (Figure 3D and data not
375 shown), but still misses many other hepatic essential genes identified by iMAP, including the 16
376 genes in gCluster IV (Figure 3D). In conclusion, iMAP seems substantially more sensitive than
377 pooled CRISPR screens. The mechanism is unclear. It is noteworthy that our experiments used
378 iMAP transgenic founder lines where the guide arrays were integrated into loci supportive of
379 robust gRNA expression (as detected by qRT-PCR). In contrast, in pooled CRISPR screens, the
380 lentiviral vectors are randomly integrated, presumably resulting in variable gRNA expression
381 whose levels might be overall below that in iMAP. In addition, iMAP mice were analyzed several
382 months after TAM administration, whereas the mice in pooled CRISPR screens were analyzed
383 3-4 weeks after lentiviral transduction, which may be insufficient for editing some target genes.

384 ### Complexity of RNA modification factors

385 Our study sheds light on context-dependent gene functions and also reveals their complexity.
386 Two issues are particularly noteworthy, each concerning tRNA modifications, as detailed below.

387

388 The first issue involves tRNA wobble uridine (U34), whose modification (mcm^5s^2) is important
389 for accurate translation of a subset of tRNAs(Schaffrath and Leidel, 2017). mcm^5s^2 comprises a
390 methoxycarbonylmethyl group at C5 position (mcm^5) introduced by ELP1-6 in conjunction with
391 ALKBH8 and TRMT112, and a thiol group at C2 position (s^2) subsequently introduced by URM1

392 in conjunction with CTU1/2, with mcm^5 being a prerequisite for s^2 (Figure 3F)(Rapino et al.,
393 2017). Of note, ELP1-6 forms the Elongator Complex, whose main function is U34 modification
394 rather than RNA polymerase elongation (Kolaj-Robin and Séraphin, 2017). iMAP-91 targets six
395 of the 11 factors in the modification pathway, namely *Elp1, Elp3, Ctu1*, *Urm1, Alkbh8* and
396 *Trmt112*. *Elp1/3* KO would eliminate all four modifications (cm^5, mcm^5, mcm^5s^2, ncm^5) present
397 on 11 tRNAs, whereas *Urm1/Ctu1* KO only mcm^5s^2 present on three (Figure 3F). Thus, one
398 might expect stronger phenotypes from *Elp1/3* KO. However, *Urm1/Ctu1* KO is each lethal
399 (MGI:1915455, 2385277), just like *Elp1/3* KO (MGI: 1914544, 1921445). In agreement with this,
400 g*Ctu1*/*Urm1* depletion was as severe as g*Elp1/3* across diverse tissues and even far more
401 severe in spermatogonia, suggesting that *Ctu1*/*Urm1* have functions beyond mcm^5s^2 writing. It is
402 also unusual that although *Alkbh8* is crucial for mcm^5s^2 just as *Urm1/Ctu1*, g16-*Alkbh8* was only
403 weakly depleted, and *Alkbh8* KO mice are alive with at most weak defects despite the complete
404 loss of mcm^5s^2 (Nakai et al., 2024; Songe-Møller et al., 2010). This is perhaps because in
405 *Alkbh8* KO mice, (n)cm5 becomes highly abundant, which might compensate for the loss of
406 mcm^5s^2 (Songe-Møller et al., 2010). In apparent conflict with this speculation, g73-*Trmt112* was
407 severely depleted contrary to g*Alkbh8*, even though *Trmt112* acts in concert with *Alkbh8* in
408 writing mcm^5 . The data suggest that *Trmt112* has functions beyond mcm^5 writing and predict
409 that *Trmt112* KO, which has not been reported, would be lethal.
410
411 The second issue regards the KEOPS complex mediating the N6-threonylcarbamoyladenosine
412 (t6A) modification at A37 of a subset of tRNAs(Srinivasan et al., 2011). KEOPS consists of five
413 subunits (LAGE3, TPRKB, OSGEP, TRP53RK and GON7) each necessary for efficient t6A
414 modification, with mutations in human orthologs each lead to Galloway-Mowat syndrome
415 (GAMOS) characterized by organ anomalies and early death (Braun et al., 2017). However,
416 although *Tprkb* and *Osgep* KO lead to preweaning lethality reminiscent of GAMOS
417 (MGI:1917036,1913496), *Lage3* KO mice are viable with only a mild defect (neutrophil number
418 change) unrelated to GAMOS (MGI:6257568), dovetailing with g38-*Lage3* depletion being much
419 less conspicuous than g70-*Tprkb*/g79-*Osgep* depletion. Thus, in contrast to man, murine *Lage3*
420 might be dispensable for t6A, or t6A dispensable for survival, which underscores species-
421 specificity of KEOPS function. Of note, our study also bears on *Trp53rk* and *Gon7*, whose KO
422 have not been reported. Specifically, murine TRP53RK is encoded by two genes, *Trp53rka* and
423 *Trp53rkb*. g47-*Trp53rkb* (but not g20-*Trp53rka*) clusters with the guides whose target gene KO
424 is lethal, predicting that *Trp53rkb* (but not *Trp53rka*) KO would likely be lethal. For *Gon7*, two
425 guides were designed: g85-*Gon7-1* inactivates *Gon7* (together with two other genes), whereas

426 g29-*Gon7-2* deletes GON7 C-terminal tail (Figure S3C). Guide depletion was widespread for
427 g85-*Gon7*-1 but restricted to spermatogonia for g*Gon7*-2. Thus, *Gon7*/related genes are
428 essential for diverse tissues, but the GON7 C-terminus is largely dispensable except for
429 spermatogonia, highlighting the unusual vulnerability of this cell type.
430

431 ## Therapeutic targets

432 First, we demonstrated the potential of iMAP in identifying targets for improving human NK-
433 based therapy. Although the actual candidates emerging from the current screen of 71 RNA
434 modification factors are limited in both quantity (only two genes) and quality (no/mild
435 potentiation of NK-mediated killing), larger-scale screens might uncover better candidates,
436 which in turn necessitates the improvement in iMAP throughput. Our preliminary data suggest
437 that a 10x-increase in the throughput (from 100 to 1000 guides/mouse line) might be feasible
438 (not shown).

439 Second, our study, together with a previous report that global *Alkbh5* KO selectively impacts
440 spermatogenesis (Zheng et al., 2013), highlights *Qtrt1/2* and *Alkbh5* as appealing male
441 contraceptive targets.
442

443 Finally, our study bears on targeted cancer therapy. Guides targeting mouse orthologs of
444 human CEGs were in general severely and ubiquitously depleted as expected, but g34-*Trmt5*
445 was a striking exception, being hardly affected in most tissues (Fig. 3D). This could reflect an
446 evolutionary divergence in *Trmt5* function (i.e., essential for human but not mice), or more
447 interestingly, a dichotomy between cancer and normal cells (i.e., cancer but not normal cells is
448 addicted to *Trmt5*). In the latter scenario, *Trmt5* inhibitors could become cancer drugs that are
449 broad-spectrum yet safe. Such drugs would be transformative; indeed, eight CEGs have been
450 FDA-approved as cancer therapy targets, but all of them are indispensable for normal cells, and
451 their inhibitors are all highly toxic and of limited applications (Rudd, 2023).

452 ## Limitations of the study

453 First, static tissues especially the brain are relatively refractory to Cas9 cleavage and thus prone
454 to false negatives, which might be addressed using Cas13 which targets RNA. Second, the
455 editing efficiencies of the guides were not validated *in vitro* except for the representative ones
456 shown in Figure 3E. High-throughput screening for Cas9 guides, which has become available
457 (Kim et al., 2020), might address this caveat and improve iMAP performance. Third, the 91-
458 guide array was constructed years ago, covering all the mouse RNA modification factors known

459 at the time, but the number has almost doubled since then, necessitating the creation of new
460 iMAP lines to catch up with the rapid progress in the field.
461
462 **Acknowledgments** We thank Dr. Kristin A. Knouse for advice, Drs Yong Cang and Peixiang
463 Ma/Guang Yang for reagents, the Molecular and Cell Biology Core Facility (MCBCF) and the
464 Molecular Imaging Core Facility (MICF) at the School of Life Science and Technology,
465 ShanghaiTech University for technical support. This study is supported by National Key R&D
466 Program of China (#2021YFA1100800, to T.C.) , Open Project of BGI-Shenzhen, Shenzhen
467 518000, China (#BGIRSZ20220001, to T.C.), and Shanghai Frontiers Science Center for
468 Biomacromolecules and Precision Medicine at ShanghaiTech University (to T.C.).

469 **Declaration of interests** The authors declare no competing interests.

470 **Data and code availability**
471 All original code has been deposited as an R package at GitHub and can be accessed using the
472 following link https://github. com/Jing-Zhengyu/iMAP. Any additional information required to
473 reanalyze the data reported in this paper is available from the lead contact upon request. The
474 source data and the codes for their plotting, together with the plasmid maps, are available at
475 https:// github.com/Jing-Zhengyu/Data-of-iMAP.
476
477 **Methods**
478 **Mice**
479 91-guide array, the ensuing transgenic line and iMAP-91 mice were generated as described.
480 The transgene sequence is available at https://github.com/Jing-Zhengyu/Data-of-iMAP). Inverse
481 PCR revealed that the transgene was inserted at Chr6:69964770(+) (coordinates based on
482 Mouse mm 39). The target genes and their guides are listed in Table S1(sheet 1). PCR primers
483 for determining transgene integration sites, checking transgene integrity, genotyping and P0
484 guide expression are in Table S1(sheet 2). Animal experiments were approved by the Animal
485 Ethics Committee at ShanghaiTech, and performed in accordance with the institutional
486 guidelines.
487
488 **Perturbation Atlas**
489 TAM treatment, tissue harvesting and PCR-NGS profiling of P0 guide were performed as
490 described (Liu et al., 2022).
491

492 **Analysis of gRNA efficiency in N2a cells**

493 We co-transfected vectors expressing gRNA (150 ng) or Cas9 (350 ng) into the mouse
494 neuroblastoma N2a cells cultured on 48-well plates. 72 h post-transfection, we extracted
495 genomic DNA, amplified 500-900-bp regions encompassing the sites targeted by gRNAs using
496 50 ng genomic DNA as templates. The amplicons were then sequenced using the Sanger
497 method and analyzed using ICE (https://www.synthego.com). PCR primers are listed in Table
498 S1 (sheet 2).

499

500 **Screens for potential therapeutic targets in tumor-infiltrating NK cells**

501 MC38 mouse colon cancer cells, gift from Yong Cang (ShanghaiTech University), maintained in
502 DMEM supplemented with 10% FBS and 1% penicillin-streptomycin, were detached using
503 0.25% trypsin, washed with PBS, resuspended at 1×10^6 cells per 100 µl PBS and injected the
504 100ul subcutaneously into the dorsal flank of 5-8 weeks-old iMAP-91 mice. Tamoxifen was
505 administered via oral gavage (0.6 g/kg) on the day of tumor inoculation. Tumor growth was
506 monitored every 2 days using calipers, and volumes calculated as $(L \times W^2)/2$,
507 where *L* and *W* represent the longest and perpendicular diameters, respectively. Tumors were
508 excised when reaching 1–1.5 cm^3, which took 18-25 days, minced and digested in RPMI-1640
509 containing 1 mg/ml collagenase IV (Sigma-Aldrich) and 0.1 mg/ml DNase I (Sigma-Aldrich) for
510 20–30 minutes at 37°C with gentle agitation. The digested samples were filtered through a 70-
511 µm strainer and cells pelleted by centrifugation at 400 ×g for 5 minutes (4°C). To identify genes
512 controlling degranulation, the cells were stained with the following antibodies: CD45.2-BB700,
513 CD3-PE-Cy7, NK1.1-APC and CD107a-APC-Cy7. $CD45.2^+CD3^-NK1.1^+$ NK cells were sorted
514 into $CD107a^{high}$ (top 30%) and $CD107a^{low/-}$ (bottom 30%) populations using a BD FACS Aria III
515 and analyzed by PCR-NGS. TNFa regulators were similarly identified, except that cells were
516 first stained for CD45.2, CD3 and NK1.1, fixed with BD Cytofix/Cytoperm™ for 20 minutes at
517 4°C, washed with BD Perm/Wash™ and stained with TNFa-PE. $TNFa^{high}$ (top 30%) and
518 $TNFa^{low/-}$ (bottom 30%) cells were then isolated for PCR-NGS.

519 **Target validation in human NK cells**

520 Human PBMCs (Rubei Biotechnology) were cultured in Corning ® Lymphocyte Serum-free
521 Medium supplemented with 10% FBS, 1% penicillin-streptomycin and 200 U/ml recombinant IL-
522 2 (Novoprotein). NK cells were expanded using an IL-21-based NK Expansion Kit (Zhongwin
523 Biotech) with stimulation on days 0 and 7. NK cell purity (>90% $CD3^-CD56^+$) was confirmed by

524 flow cytometry on day 10. K562 leukemia cells stably expressing firefly luciferase (gift from
525 Guang Yang, ShanghaiTech) (Ma et al., 2021) were maintained in RPMI-1640 with 10% FBS
526 and 1% penicillin-streptomycin under standard conditions. RNP was assembled by incubating
527 40 pm each of recombinant Cas9 (Sino Biological) and sgRNA or non-targeting control (Table
528 S1 sheet 3) at 37°C for 15 min. RNP was mixed with 3×10^6 NK cells resuspended in 20 μl P3
529 Primary Cell Solution (Lonza) before electroporation using a 4D-Nucleofector™ (program CM-
530 137). 48 h post-transfection, successful editing was confirmed by PCR-Sanger sequencing, and
531 NK (0.2×10^6 /well) were co-incubated with K562 (0.4×10^6 /well) cells for 4-6 h in 96-well plates
532 in PBMC culture media. To assess K562 lysis, cells were washed with PBS, resuspended in
533 media containing cell-permeable D-Luciferin potassium salt (150 μg/ml, Beyotime) and
534 incubated at 37℃ for 5 min before measuring luminescence using an Infinite M200 Pro plate
535 reader (Tecan) (Ma et al., 2021). The lysis rate was calculated as (1-X/N) %, where X is the
536 luminescence intensity of K562 cells co-cultured with electroporated NK cells, and N is that of
537 K562 cells never exposed to NK cells. CD107a and cellular TNFα were detected by FACS,
538 whereas TNFα secreted to the media by ELISA.
539

540 ## References

541 Braun, C.J., Adames, A.C., Saur, D., Rad, R., 2022. Tutorial: design and execution of CRISPR in vivo screens.
542 Nat Protoc 17, 1903—1925. https://doi.org/10.1038/s41596-022-00700-y
543 Braun, D.A., Rao, J., Mollet, G., Schapiro, D., Daugeron, M.-C., Tan, W., Gribouval, O., Boyer, O., Revy, P.,
544 Jobst-Schwan, T., Schmidt, J.M., Lawson, J.A., Schanze, D., Ashraf, S., Ullmann, J.F.P., Hoogstraten,
545 C.A., Boddaert, N., Collinet, B., Martin, G., Liger, D., Lovric, S., Furlano, M., Guerrera, I.C., Sanchez-
546 Ferras, O., Hu, J.F., Boschat, A.-C., Sanquer, S., Menten, B., Vergult, S., De Rocker, N., Airik, M.,
547 Hermle, T., Shril, S., Widmeier, E., Gee, H.Y., Choi, W.-I., Sadowski, C.E., Pabst, W.L., Warejko, J.K.,
548 Daga, A., Basta, T., Matejas, V., Scharmann, K., Kienast, S.D., Behnam, B., Beeson, B., Begtrup, A.,
549 Bruce, M., Ch'ng, G.-S., Lin, S.-P., Chang, J.-H., Chen, C.-H., Cho, M.T., Gaffney, P.M., Gipson, P.E.,
550 Hsu, C.-H., Kari, J.A., Ke, Y.-Y., Kiraly-Borri, C., Lai, W., Lemyre, E., Littlejohn, R.O., Masri, A.,
551 Moghtaderi, M., Nakamura, K., Ozaltin, F., Praet, M., Prasad, C., Prytula, A., Roeder, E.R., Rump, P.,
552 Schnur, R.E., Shiihara, T., Sinha, M.D., Soliman, N.A., Soulami, K., Sweetser, D.A., Tsai, W.-H., Tsai, J.-
553 D., Topaloglu, R., Vester, U., Viskochil, D.H., Vatanavicharn, N., Waxler, J.L., Wierenga, K.J., Wolf,
554 M.T.F., Wong, S.-N., Leidel, S.A., Truglio, G., Dedon, P.C., Poduri, A., Mane, S., Lifton, R.P., Bouchard,
555 M., Kannu, P., Chitayat, D., Magen, D., Callewaert, B., van Tilbeurgh, H., Zenker, M., Antignac, C.,
556 Hildebrandt, F., 2017. Mutations in KEOPS-complex genes cause nephrotic syndrome with primary
557 microcephaly. Nat Genet 49, 1529—1538. https://doi.org/10.1038/ng.3933

558 Cai, H., Winslow, M.M., 2022. A new system for multiplexed mosaic analysis of gene function in the mouse.
559 Cell Reports Methods 2, 100295. https://doi.org/10.1016/j.crmeth.2022.100295
560 Cappannini, A., Ray, A., Purta, E., Mukherjee, S., Boccaletto, P., Moafinejad, S.N., Lechner, A., Barchet, C.,
561 Klaholz, B.P., Stefaniak, F., Bujnicki, J.M., 2024. MODOMICS: a database of RNA modifications and
562 related information. 2023 update. Nucleic Acids Res 52, D239—D244.
563 https://doi.org/10.1093/nar/gkad1083
564 Chow, R.D., Chen, S., 2018. Cancer CRISPR screens in vivo. Trends Cancer 4, 349—358.
565 https://doi.org/10.1016/j.trecan.2018.03.002
566 Coënon, L., Geindreau, M., Ghiringhelli, F., Villalba, M., Bruchard, M., 2024. Natural Killer cells at the frontline in
567 the fight against cancer. Cell Death Dis 15, 1—14. https://doi.org/10.1038/s41419-024-06976-0
568 Cui, L., Ma, R., Cai, J., Guo, C., Chen, Z., Yao, L., Wang, Y., Fan, R., Wang, X., Shi, Y., 2022. RNA modifications:
569 importance in immune cell biology and related diseases. Sig Transduct Target Ther 7, 1—26.
570 https://doi.org/10.1038/s41392-022-01175-9
571 Fallon, T.K., Knouse, K.A., 2025. A roadmap toward genome-wide CRISPR screening throughout the organism.
572 Cell Genom 5, 100777. https://doi.org/10.1016/j.xgen.2025.100777
573 González-Flores, D., Rodríguez, A.B., Pariente, J.A., 2014. TNFα-induced apoptosis in human myeloid cell lines
574 HL-60 and K562 is dependent of intracellular ROS generation. Mol Cell Biochem 390, 281—287.
575 https://doi.org/10.1007/s11010-014-1979-5
576 Hart, T., Tong, A.H.Y., Chan, K., Leeuwen, J.V., Seetharaman, A., Aregger, M., Chandrashekhar, M., Hustedt, N.,
577 Seth, S., Noonan, A., Habsid, A., Sizova, O., Nedyalkova, L., Climie, R., Tworzyanski, L., Lawson, K.,
578 Sartori, M.A., Alibeh, S., Tieu, D., Masud, S., Mero, P., Weiss, A., Brown, K.R., Usaj, M., Billmann, M.,
579 Rahman, M., Costanzo, M., Myers, C.L., Andrews, B.J., Boone, C., Durocher, D., Moffat, J., 2017.
580 Evaluation and Design of Genome-Wide CRISPR/SpCas9 Knockout Screens. G3: Genes, Genomes,
581 Genetics 7, 2719—2727. https://doi.org/10.1534/g3.117.041277
582 Jin, X., Simmons, S.K., Guo, A., Shetty, A.S., Ko, M., Nguyen, L., Jokhi, V., Robinson, E., Oyler, P., Curry, N.,
583 Deangeli, G., Lodato, S., Levin, J.Z., Regev, A., Zhang, F., Arlotta, P., 2020. In vivo Perturb-Seq reveals
584 neuronal and glial abnormalities associated with autism risk genes. Science 370.
585 https://doi.org/10.1126/science.aaz6063
586 Johannsson, S., Neumann, P., Ficner, R., 2018. Crystal Structure of the Human tRNA Guanine Transglycosylase
587 Catalytic Subunit QTRT1. Biomolecules 8, 81. https://doi.org/10.3390/biom8030081
588 Joung, J., Konermann, S., Gootenberg, J.S., Abudayyeh, O.O., Platt, R.J., Brigham, M.D., Sanjana, N.E., Zhang,
589 F., 2017. Genome-scale CRISPR-Cas9 knockout and transcriptional activation screening. Nature
590 Protocols 12, 828—863. https://doi.org/10.1038/nprot.2017.016
591 Keys, H.R., Knouse, K.A., 2022. Genome-scale CRISPR screening in a single mouse liver. Cell Genom 2, 100217.
592 https://doi.org/10.1016/j.xgen.2022.100217
593 Kim, H.K., Lee, S., Kim, Y., Park, J., Min, S., Choi, J.W., Huang, T.P., Yoon, S., Liu, D.R., Kim, H.H., 2020. High-
594 throughput analysis of the activities of xCas9, SpCas9-NG and SpCas9 at matched and mismatched
595 target sequences in human cells. Nat Biomed Eng 4, 111—124. https://doi.org/10.1038/s41551-019-
596 0505-1

597 Kolaj-Robin, O., Séraphin, B., 2017. Structures and Activities of the Elongator Complex and Its Cofactors.
598 Enzymes 41, 117—149. https://doi.org/10.1016/bs.enz.2017.03.001
599 Kuhn, M., Santinha, A.J., Platt, R.J., 2021. Moving from in vitro to in vivo CRISPR screens. Gene and Genome
600 Editing 2, 100008. https://doi.org/10.1016/j.ggedit.2021.100008
601 Ladang, A., Rapino, F., Heukamp, L.C., Tharun, L., Shostak, K., Hermand, D., Delaunay, S., Klevernic, I., Jiang, Z.,
602 Jacques, N., Jamart, D., Migeot, V., Florin, A., Göktuna, S., Malgrange, B., Sansom, O.J., Nguyen, L.,
603 Büttner, R., Close, P., Chariot, A., 2015. Elp3 drives Wnt-dependent tumor initiation and regeneration
604 in the intestine. J Exp Med 212, 2057—2075. https://doi.org/10.1084/jem.20142288
605 Li, J., Wang, L., Hahn, Q., Nowak, R.P., Viennet, T., Orellana, E.A., Roy Burman, S.S., Yue, H., Hunkeler, M.,
606 Fontana, P., Wu, H., Arthanari, H., Fischer, E.S., Gregory, R.I., 2023. Structural basis of regulated m7G
607 tRNA modification by METTL1—WDR4. Nature 613, 391—397. https://doi.org/10.1038/s41586-022-
608 05566-4
609 Liu, B., Jing, Z., Zhang, X., Chen, Y., Mao, S., Kaundal, R., Zou, Y., Wei, G., Zang, Y., Wang, X., Lin, W., Di, M.,
610 Sun, Y., Chen, Q., Li, Y., Xia, J., Sun, J., Lin, C.-P., Huang, X., Chi, T., 2022. Large-scale multiplexed
611 mosaic CRISPR perturbation in the whole organism. Cell 185, 3008-3024.e16.
612 https://doi.org/10.1016/j.cell.2022.06.039
613 Ma, P., Ren, P., Zhang, C., Tang, J., Yu, Z., Zhu, X., Fan, K., Li, G., Zhu, W., Sang, W., Min, C., Chen, W., Huang,
614 X., Yang, G., Lerner, R.A., 2021. Avidity-Based Selection of Tissue-Specific CAR-T Cells from a
615 Combinatorial Cellular Library of CARs. Adv Sci (Weinh) 8, 2003091.
616 https://doi.org/10.1002/advs.202003091
617 Maskalenko, N.A., Zhigarev, D., Campbell, K.S., 2022. Harnessing natural killer cells for cancer immunotherapy:
618 dispatching the first responders. Nat Rev Drug Discov 21, 559—577. https://doi.org/10.1038/s41573-
619 022-00413-7
620 Nakai, M., Hase, H., Zhao, Y., Okawa, K., Honda, K., Ikuma, K., Kitae, K., Tsujikawa, K., 2024. RNA-modifying
621 enzyme Alkbh8 is involved in mouse embryonic development. iScience 27, 110777.
622 https://doi.org/10.1016/j.isci.2024.110777
623 Noguchi, Y., Onodera, Y., Miyamoto, T., Maruoka, M., Kosako, H., Suzuki, J., 2024. In vivo CRISPR screening
624 directly targeting testicular cells. Cell Genom 4, 100510. https://doi.org/10.1016/j.xgen.2024.100510
625 Park, K.-H., Park, H., Kim, M., Kim, Y., Han, K., Oh, E.-J., n.d. Evaluation of NK Cell Function by
626 Flowcytometric Measurement and Impedance Based Assay Using Real-Time Cell Electronic Sensing
627 System. https://doi.org/10.1155/2013/210726
628 Qiu, L., Jing, Q., Li, Y., Han, J., 2023. RNA modification: mechanisms and therapeutic targets. Mol Biomed 4,
629 25. https://doi.org/10.1186/s43556-023-00139-x
630 Rakovich, T., Boland, C., Bernstein, I., Chikwana, V.M., Iwata-Reuyl, D., Kelly, V.P., 2011. Queuosine deficiency
631 in eukaryotes compromises tyrosine production through increased tetrahydrobiopterin oxidation. J Biol
632 Chem 286, 19354—19363. https://doi.org/10.1074/jbc.M111.219576
633 Rapino, F., Delaunay, S., Zhou, Z., Chariot, A., Close, P., 2017. tRNA Modification: Is Cancer Having a Wobble?
634 Trends Cancer 3, 249—252. https://doi.org/10.1016/j.trecan.2017.02.004

635 Regev, A., Teichmann, S.A., Lander, E.S., Amit, I., Benoist, C., Birney, E., Bodenmiller, B., Campbell, P., Carninci,
636 P., Clatworthy, M., Clevers, H., Deplancke, B., Dunham, I., Eberwine, J., Eils, R., Enard, W., Farmer, A.,
637 Fugger, L., Göttgens, B., Hacohen, N., Haniffa, M., Hemberg, M., Kim, S., Klenerman, P., Kriegstein, A.,
638 Lein, E., Linnarsson, S., Lundberg, E., Lundeberg, J., Majumder, P., Marioni, J.C., Merad, M., Mhlanga,
639 M., Nawijn, M., Netea, M., Nolan, G., Pe'er, D., Phillipakis, A., Ponting, C.P., Quake, S., Reik, W.,
640 Rozenblatt-Rosen, O., Sanes, J., Satija, R., Schumacher, T.N., Shalek, A., Shapiro, E., Sharma, P., Shin,
641 J.W., Stegle, O., Stratton, M., Stubbington, M.J.T., Theis, F.J., Uhlen, M., van Oudenaarden, A., Wagner,
642 A., Watt, F., Weissman, J., Wold, B., Xavier, R., Yosef, N., Human Cell Atlas Meeting Participants, 2017.
643 The Human Cell Atlas. Elife 6, e27041. https://doi.org/10.7554/eLife.27041
644 Rogers, Z.N., McFarland, C.D., Winters, I.P., Naranjo, S., Chuang, C.-H., Petrov, D., Winslow, M.M., 2017. A
645 quantitative and multiplexed approach to uncover the fitness landscape of tumor suppression in vivo.
646 Nat. Methods 14, 737—742. https://doi.org/10.1038/nmeth.4297
647 Rogers, Z.N., McFarland, C.D., Winters, I.P., Seoane, J.A., Brady, J.J., Yoon, S., Curtis, C., Petrov, D.A., Winslow,
648 M.M., 2018. Mapping the in vivo fitness landscape of lung adenocarcinoma tumor suppression in mice.
649 Nat. Genet. 50, 483—486. https://doi.org/10.1038/s41588-018-0083-2
650 Rood, J.E., Hupalowska, A., Regev, A., 2024. Toward a foundation model of causal cell and tissue biology with
651 a Perturbation Cell and Tissue Atlas. Cell 187, 4520—4545. https://doi.org/10.1016/j.cell.2024.07.035
652 Rood, J.E., Maartens, A., Hupalowska, A., Teichmann, S.A., Regev, A., 2022. Impact of the Human Cell Atlas on
653 medicine. Nat Med 28, 2486—2496. https://doi.org/10.1038/s41591-022-02104-7
654 Rudd, S.G., 2023. Targeting pan-essential pathways in cancer with cytotoxic chemotherapy: challenges and
655 opportunities. Cancer Chemother Pharmacol 92, 241—251. https://doi.org/10.1007/s00280-023-
656 04562-3
657 Santinha, A.J., Klingler, E., Kuhn, M., Farouni, R., Lagler, S., Kalamakis, G., Lischetti, U., Jabaudon, D., Platt,
658 R.J., 2023. Transcriptional linkage analysis with in vivo AAV-Perturb-seq. Nature 622, 367—375.
659 https://doi.org/10.1038/s41586-023-06570-y
660 Schaffrath, R., Leidel, S.A., 2017. Wobble uridine modifications-a reason to live, a reason to die?! RNA Biol 14,
661 1209—1222. https://doi.org/10.1080/15476286.2017.1295204
662 Schmucker, S., Martelli, A., Colin, F., Page, A., Wattenhofer-Donzé, M., Reutenauer, L., Puccio, H., 2011.
663 Mammalian Frataxin: An Essential Function for Cellular Viability through an Interaction with a
664 Preformed ISCU/NFS1/ISD11 Iron-Sulfur Assembly Complex. PLoS One 6, e16199.
665 https://doi.org/10.1371/journal.pone.0016199
666 Shi, H., Doench, J.G., Chi, H., 2023. CRISPR screens for functional interrogation of immunity. Nat Rev Immunol
667 23, 363—380. https://doi.org/10.1038/s41577-022-00802-4
668 Sievers, K., Neumann, P., Sušac, L., Da Vela, S., Graewert, M., Trowitzsch, S., Svergun, D., Tampé, R., Ficner, R.,
669 2024. Structural and functional insights into tRNA recognition by human tRNA guanine
670 transglycosylase. Structure 32, 316-327.e5. https://doi.org/10.1016/j.str.2023.12.006
671 Songe-Møller, L., van den Born, E., Leihne, V., Vågbø, C.B., Kristoffersen, T., Krokan, H.E., Kirpekar, F., Falnes,
672 P.Ø., Klungland, A., 2010. Mammalian ALKBH8 possesses tRNA methyltransferase activity required for

673 the biogenesis of multiple wobble uridine modifications implicated in translational decoding. Mol Cell
674 Biol 30, 1814—1827. https://doi.org/10.1128/MCB.01602-09
675 Srinivasan, M., Mehta, P., Yu, Y., Prugar, E., Koonin, E.V., Karzai, A.W., Sternglanz, R., 2011. The highly
676 conserved KEOPS/EKC complex is essential for a universal tRNA modification, t6A. EMBO J 30, 873—
677 881. https://doi.org/10.1038/emboj.2010.343
678 Sun, Y., Lin, W., Kaundal, R., Chi, T., 2023. iMAPping the Perturb-Atlas. Life Medicine 2, lnac057.
679 https://doi.org/10.1093/lifemedi/lnac057
680 Wang, P., Doxtader, K.A., Nam, Y., 2016. Structural Basis for Cooperative Function of Mettl3 and Mettl14
681 Methyltransferases. Mol Cell 63, 306—317. https://doi.org/10.1016/j.molcel.2016.05.041
682 Wang, Y., Wang, Jing, Li, X., Xiong, X., Wang, Jianyi, Zhou, Z., Zhu, X., Gu, Y., Dominissini, D., He, L., Tian, Y.,
683 Yi, C., Fan, Z., 2021. N1-methyladenosine methylation in tRNA drives liver tumourigenesis by regulating
684 cholesterol metabolism. Nat Commun 12, 6314. https://doi.org/10.1038/s41467-021-26718-6
685 Wertz, M.H., Mitchem, M.R., Pineda, S.S., Hachigian, L.J., Lee, H., Lau, V., Powers, A., Kulicke, R., Madan, G.K.,
686 Colic, M., Therrien, M., Vernon, A., Beja-Glasser, V.F., Hegde, M., Gao, F., Kellis, M., Hart, T., Doench,
687 J.G., Heiman, M., 2020. Genome-wide In Vivo CNS Screening Identifies Genes that Modify CNS
688 Neuronal Survival and mHTT Toxicity. Neuron 106, 76-89.e8.
689 https://doi.org/10.1016/j.neuron.2020.01.004
690 Wu, Y., Wei, F.-Y., Kawarada, L., Suzuki, Takeo, Araki, K., Komohara, Y., Fujimura, A., Kaitsuka, T., Takeya, M.,
691 Oike, Y., Suzuki, Tsutomu, Tomizawa, K., 2016. Mtu1-Mediated Thiouridine Formation of Mitochondrial
692 tRNAs Is Required for Mitochondrial Translation and Is Involved in Reversible Infantile Liver Injury.
693 PLOS Genetics 12, e1006355. https://doi.org/10.1371/journal.pgen.1006355
694 Yi, C., Yang, J., 2023. RNA Modifications and Epitranscriptomics. Genomics, Proteomics & Bioinformatics 21,
695 675—677. https://doi.org/10.1016/j.gpb.2023.10.002
696 Zheng, G., Dahl, J.A., Niu, Y., Fedorcsak, P., Huang, C.-M., Li, C.J., Vågbø, C.B., Shi, Y., Wang, W.-L., Song, S.-
697 H., Lu, Z., Bosmans, R.P.G., Dai, Q., Hao, Y.-J., Yang, X., Zhao, W.-M., Tong, W.-M., Wang, X.-J.,
698 Bogdan, F., Furu, K., Fu, Y., Jia, G., Zhao, X., Liu, J., Krokan, H.E., Klungland, A., Yang, Y.-G., He, C.,
699 2013. ALKBH5 is a mammalian RNA demethylase that impacts RNA metabolism and mouse fertility.
700 Mol Cell 49, 18—29. https://doi.org/10.1016/j.molcel.2012.10.015
701 Zheng, X., Wu, B., Liu, Y., Simmons, S.K., Kim, K., Clarke, G.S., Ashiq, A., Park, J., Li, J., Wang, Z., Tong, L.,
702 Wang, Q., Rajamani, K.T., Muñoz-Castañeda, R., Mu, S., Qi, T., Zhang, Y., Ngiam, Z.C., Ohte, N.,
703 Hanashima, C., Wu, Z., Xu, X., Levin, J.Z., Jin, X., 2024. Massively parallel in vivo Perturb-seq reveals
704 cell-type-specific transcriptional networks in cortical development. Cell 187, 3236-3248.e21.
705 https://doi.org/10.1016/j.cell.2024.04.050
706

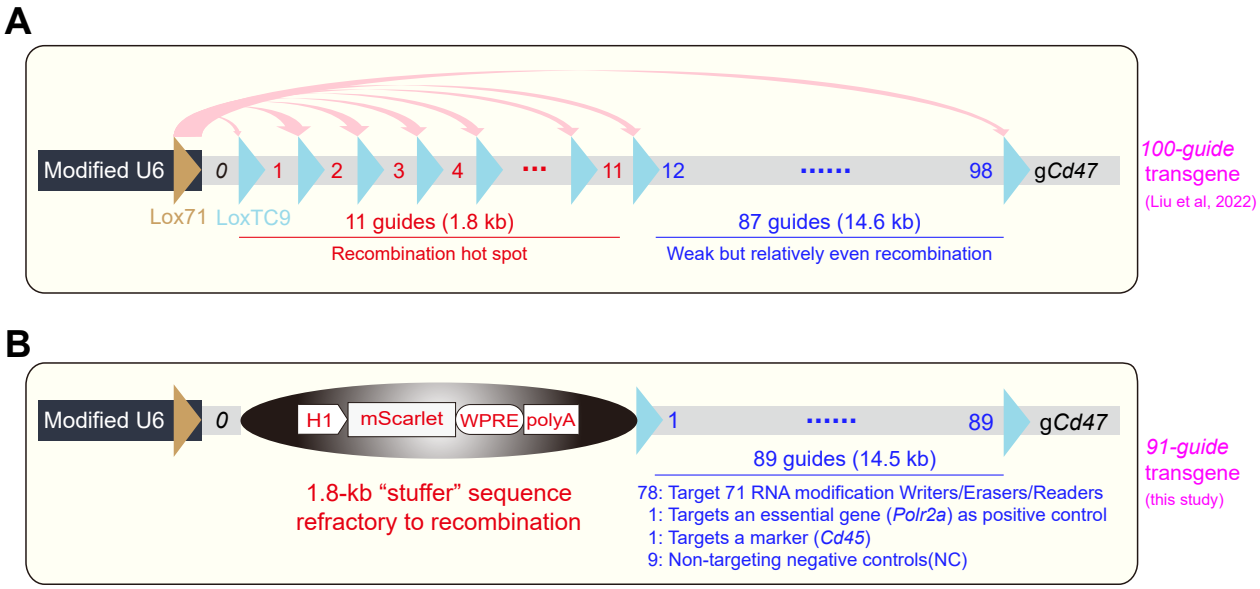

Figure 1. Strategy for minimizing recombination bias
(A) First-generation iMAP transgene. Lox71 and TC9 are LoxP variants embedded in the U6 promoter and precede each gRNA-coding gene ("guide"), respectively. The guide at Position 0 (P0) is g*Cd19* (not shown). The last guide (g*Cd47*) facilitates PCR-NGS quantification of recombined products. Following recombination between Lox71 and a LoxTC9 preceding a guide, the intervening sequence is deleted, re-locating the guide to P0 for transcription. The recombination between Lox71 and the series of LoxTC9 sites is biased toward the proximal LoxTC9 sites except the first site, perhaps due to steric hindrance created by the transcription machinery at U6 promoter.
(B) Optimized configuration. The "stuffer" harbors an expression cassette for monitoring U6 promoter activity, which proved unsuccessful (Figure S1D). The guide at Position 0(P0) is g*Cd19* (not shown). The target genes and gRNAs are listed in Table S1.

Fig. 2

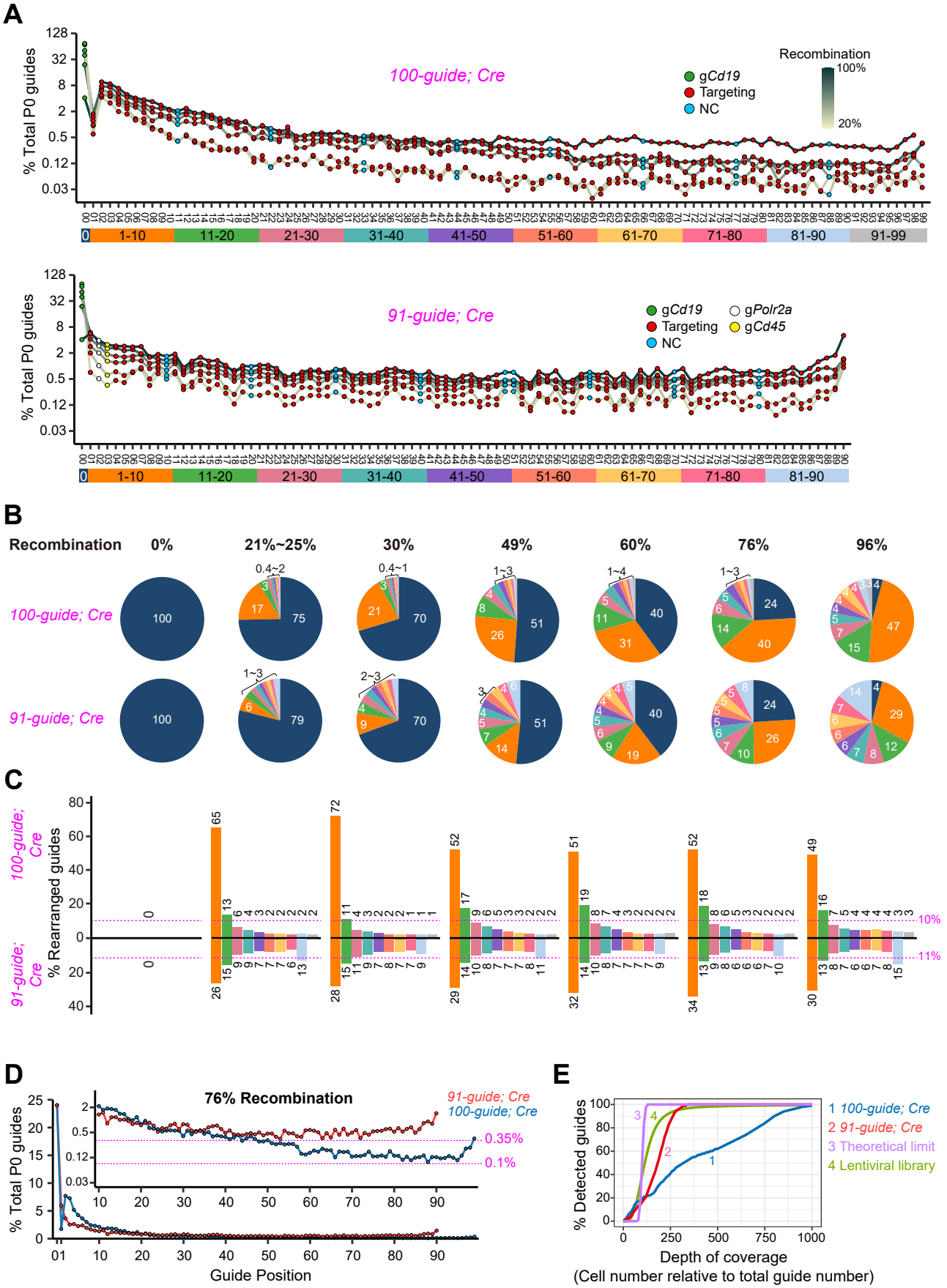
A
100-guide; Cre
% Total P0 guides
gCd19
Targeting
NC
Recombination
100%
20%
1-10
11-20
21-30
31-40
41-50
51-60
61-70
71-80
81-90
91-99
91-guide; Cre
gPolr2a
gCd45
B
Recombination
0%
21%~25%
30%
49%
60%
76%
96%
100-guide; Cre
91-guide; Cre
C
% Rearranged guides
10%
11%
D
76% Recombination
0.35%
0.1%
Guide Position
E
% Detected guides
1 100-guide; Cre
2 91-guide; Cre
3 Theoretical limit
4 Lentiviral library
Depth of coverage
(Cell number relative to total guide number)

Figure 2. Improved guide representation in the optimized iMAP transgene

(A) P0 guide profiles as a function of recombination extents. *100-guide; Cre* (top) or *91-guide; Cre* (bottom) mice were treated with increasing doses of TAM before analysis of various organs, and samples with progressive recombination, as measured by *gCd19* deletion, are selected for display. Shown is the relative abundance of individual guide among all P0 guides, with each line representing a sample. The guides are arranged according to their positions on the array. An ID number is appended to each guide if several guides are designed for the same genes. Two identical non-targeting guides (50-NC5, 51-NC5) were inadvertently built into the *91-guide* array. The colored bar at the bottom specifies the groups of guides whose abundance is analyzed in B. Source data in Table S2.

(B) Same as A, but displays the guides as groups defined by the colored bar in A. The values above the pies indicate the extent of *gCd19* deletion; e.g., the third pie shows 70% of *gCd19* survived recombination, translating to 30% deletion. The upper and lower pie charts are paired.

(C) Same as B but displays guide abundance relative to all the re-arranged P0 guides (hence with *gCd19* excluded), which better exposes the bias in recombination. The dotted lines denote the theoretical guide abundance if the recombination is absolutely even.

(D) Same as A, but compares a pair of samples with 76% recombination from the two mouse lines. The inset displays the distal and hence low-abundance guides.

(E) Monte Carlo simulation of guide detectability as a function of number of the cells sampled. The simulation is based on actual guide representation after recombination (#1-2) or viral transduction (#4; data averaged from two lentiviral libraries reported in (Uijttewaal et al., 2024)).

Fig. 3

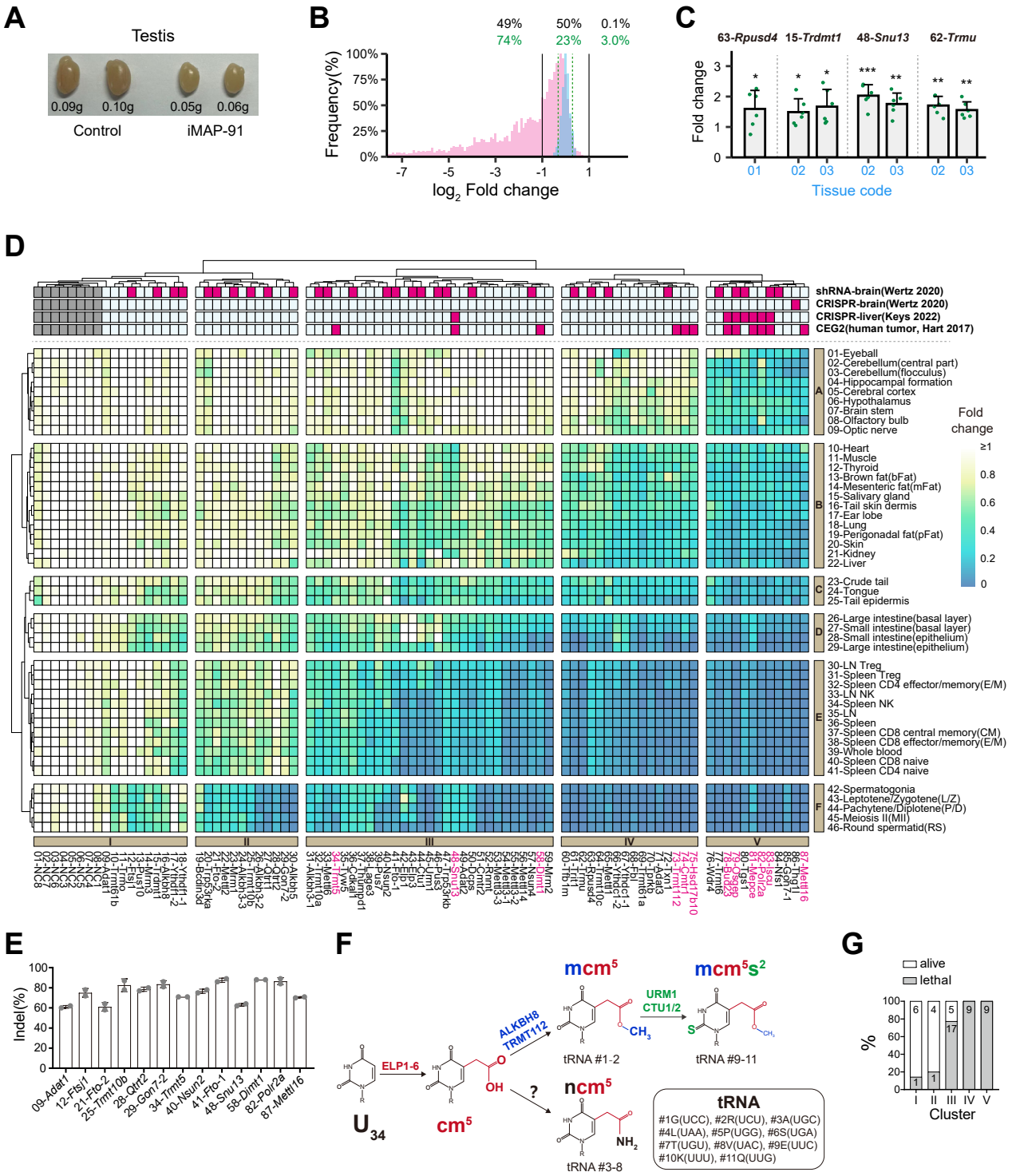
A
Testis
0.09g
0.10g
0.05g
0.06g
Control
iMAP-91
B
49%
50%
0.1%
74%
23%
3.0%
Frequency(%)
100%
75%
50%
25%
0%
-7
-5
-3
-1
1
log2 Fold change
C
63-Rpusd4
15-Trdmt1
48-Snu13
62-Trmu
Fold change
Tissue code
01
02
03
02
03
02
03
D
shRNA-brain(Wertz 2020)
CRISPR-brain(Wertz 2020)
CRISPR-liver(Keys 2022)
CEG2(human tumor, Hart 2017)
01-Eyeball
02-Cerebellum(central part)
03-Cerebellum(flocculus)
04-Hippocampal formation
05-Cerebral cortex
06-Hypothalamus
07-Brain stem
08-Olfactory bulb
09-Optic nerve
10-Heart
11-Muscle
12-Thyroid
13-Brown fat(bFat)
14-Mesenteric fat(mFat)
15-Salivary gland
16-Tail skin dermis
17-Ear lobe
18-Lung
19-Perigonadal fat(pFat)
20-Skin
21-Kidney
22-Liver
23-Crude tail
24-Tongue
25-Tail epidermis
26-Large intestine(basal layer)
27-Small intestine(basal layer)
28-Small intestine(epithelium)
29-Large intestine(epithelium)
30-LN Treg
31-Spleen Treg
32-Spleen CD4 effector/memory(E/M)
33-LN NK
34-Spleen NK
35-LN
36-Spleen
37-Spleen CD8 central memory(CM)
38-Spleen CD8 effector/memory(E/M)
39-Whole blood
40-Spleen CD8 naive
41-Spleen CD4 naive
42-Spermatogonia
43-Leptotene/Zygotene(L/Z)
44-Pachytene/Diplotene(P/D)
45-Meiosis II(MII)
46-Round spermatid(RS)
Fold change
≥1
0.8
0.6
0.4
0.2
0
E
Indel(%)
09-Adat1
12-Fisj1
21-Fto-2
25-Trmt10b
28-Qtrt2
29-Gon7-2
34-Trmt5
40-Nsun2
41-Fto-1
48-Snu13
58-Dimt1
82-Polr2a
87-Mettl16
F
U34
ELP1-6
cm5
ALKBH8
TRMT112
mcm5
tRNA #1-2
URM1
CTU1/2
mcm5s2
tRNA #9-11
?
ncm5
tRNA #3-8
tRNA
#1G(UCC), #2R(UCU), #3A(UGC)
#4L(UAA), #5P(UGG), #6S(UGA)
#7T(UGU), #8V(UAC), #9E(UUC)
#10K(UUU), #11Q(UUG)
G
alive
lethal
%
Cluster

Figure 3. iMAP-91 characterization

(A) Atrophic testes.

(B) Frequency distribution of the fold-changes for the 79 targeting (pink) and eight NC (cyan) guides across 46 tissues. Black lines mark 2-fold changes, whereas the green lines indicate the 5th and 95th percentiles of gNC values.

(C) Guide enrichment. Tissue code 01, 02, 03 refers to eyeball, cerebellar central part and cerebellar flocculus, respectively, as specified in (D). Values are mean ± SD. *$p < 0.05$, **$p < 0.01$, ***$p< 0.001$, Student's t-test.

(D) Cluster analysis of guide depletion. Displayed are 87 guides comprising all the guides targeting the 71 RNA modification factors together with all the gNC except the inadvertently duplicated one. Essentiality of the 71 genes per literature is indicated at the top of the heatmap, where shRNA-brain and CRISPR-brain refer to, respectively, the shRNA- and sgRNA-based genomewide *in situ* screens for neuronal essential genes in the mouse striatum (Wertz et al., 2020), CRISPR-liver is a genomewide *in situ* screen for liver essential genes (Keys and Knouse, 2022), and CEG2 the core essential gene set identified in human tumor cell lines (Hart et al., 2017). CEG2 guides are colored pink. The data points are averaged from 2 to 6 (mostly 5-6) biological replicates.Source data in Table S3.

(E) Editing rates of representative gRNAs selected from iMAP-91. gRNAs and Cas9 were co-expressed in N2a cells in duplicates before indel quantification.

(F) Cascade reaction leading to tRNA-U34 modifications (Rapino et al., 2017b).

(G) Guide clustering coincides with the phenotypes of global single-gene KO mice. Analyzed are the genes whose KO phenotypes are available from MGI. The number of genes in each category is indicated. Source data in Table S3 (sheet 2).

Fig. 4

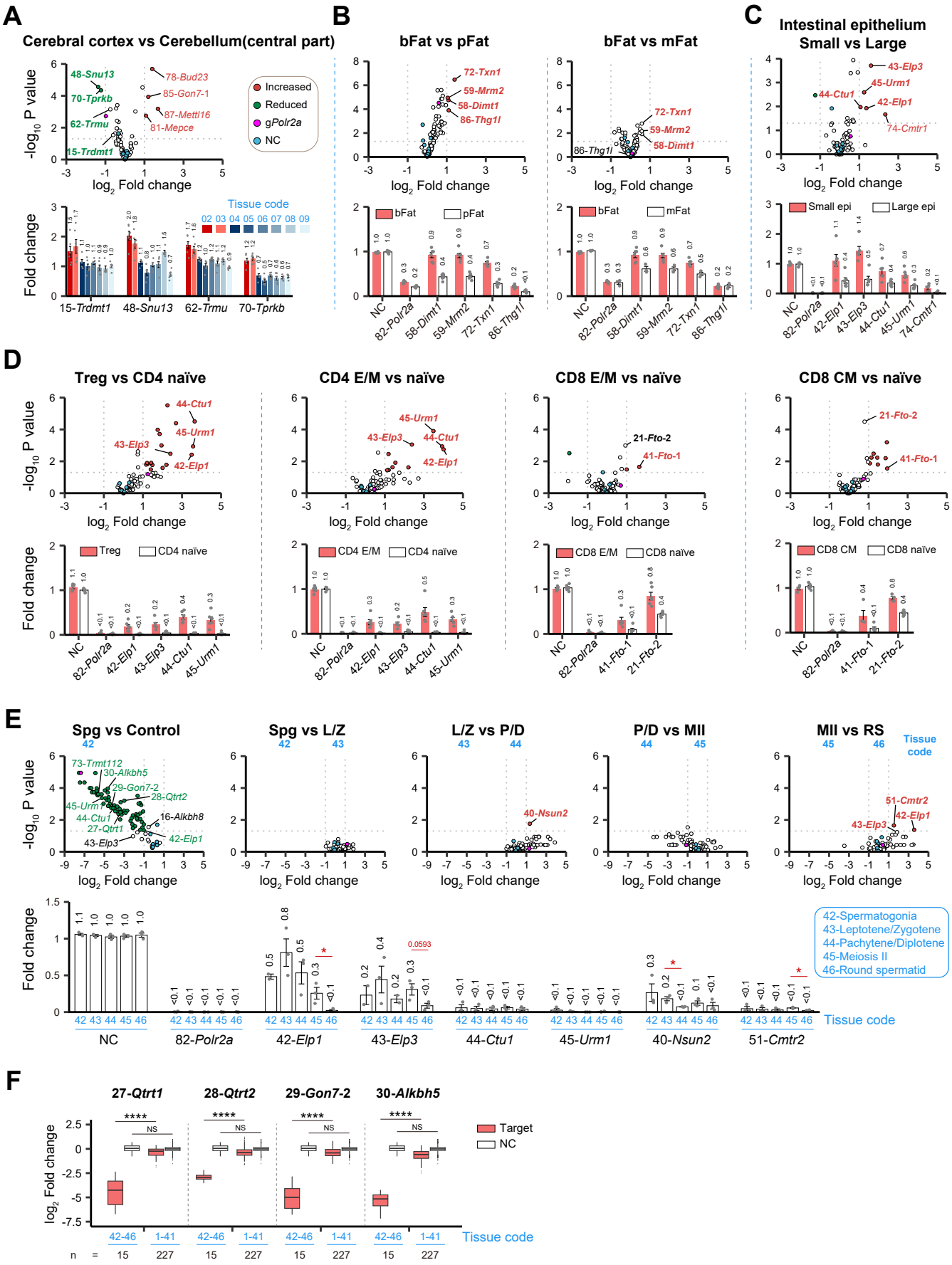
A
Cerebral cortex vs Cerebellum(central part)
-log10 P value
log2 Fold change
48-Snu13
70-Tprkb
62-Trmu
15-Trdmt1
78-Bud23
85-Gon7-1
87-Mettl16
81-Mepce
Increased
Reduced
gPolr2a
NC
Fold change
Tissue code
02 03 04 05 06 07 08 09
15-Trdmt1
48-Snu13
62-Trmu
70-Tprkb
B
bFat vs pFat
72-Txn1
59-Mrm2
58-Dimt1
86-Thg1l
bFat
pFat
bFat vs mFat
mFat
NC
82-Polr2a
58-Dimt1
59-Mrm2
72-Txn1
86-Thg1l
C
Intestinal epithelium
Small vs Large
43-Elp3
45-Urm1
44-Ctu1
42-Elp1
74-Cmtr1
Small epi
Large epi
NC
82-Polr2a
42-Elp1
43-Elp3
44-Ctu1
45-Urm1
74-Cmtr1
D
Treg vs CD4 naïve
44-Ctu1
45-Urm1
43-Elp3
42-Elp1
Treg
CD4 naïve
CD4 E/M vs naïve
CD4 E/M
CD8 E/M vs naïve
21-Fto-2
41-Fto-1
CD8 E/M
CD8 naïve
CD8 CM vs naïve
CD8 CM
NC
82-Polr2a
42-Elp1
43-Elp3
44-Ctu1
45-Urm1
41-Fto-1
21-Fto-2
E
Spg vs Control
Spg vs L/Z
L/Z vs P/D
P/D vs MII
MII vs RS
Tissue code
73-Trmt112
30-Alkbh5
29-Gon7-2
28-Qtrt2
45-Urm1
44-Ctu1
27-Qtrt1
43-Elp3
16-Alkbh8
42-Elp1
40-Nsun2
51-Cmtr2
42-Spermatogonia
43-Leptotene/Zygotene
44-Pachytene/Diplotene
45-Meiosis II
46-Round spermatid
0.0593
NC
82-Polr2a
42-Elp1
43-Elp3
44-Ctu1
45-Urm1
40-Nsun2
51-Cmtr2
Tissue code
F
27-Qtrt1
28-Qtrt2
29-Gon7-2
30-Alkbh5
****
NS
Target
NC
log2 Fold change
42-46
1-41
Tissue code
n = 15 227

Figure 4. Mining the heatmap data

(A-D) Comparing tissue pairs. Shown are differentially represented guides (top) and their absolute abundance normalized to *91-guide; Cre* control mice (bottom). Red and green dots within the top plots indicate significant enrichment and depletion, respectively (fold-change> 2, $p<0.05$).

(E) Guide depletion during spermatogenesis. Same as A-D, but focusing on the male germline.

(F) Germline-specific guide depletion. Values are mean ± SD, n = 15–227, each data point being a guide -tissue-replicate combination. ****$p < 0.0001$.

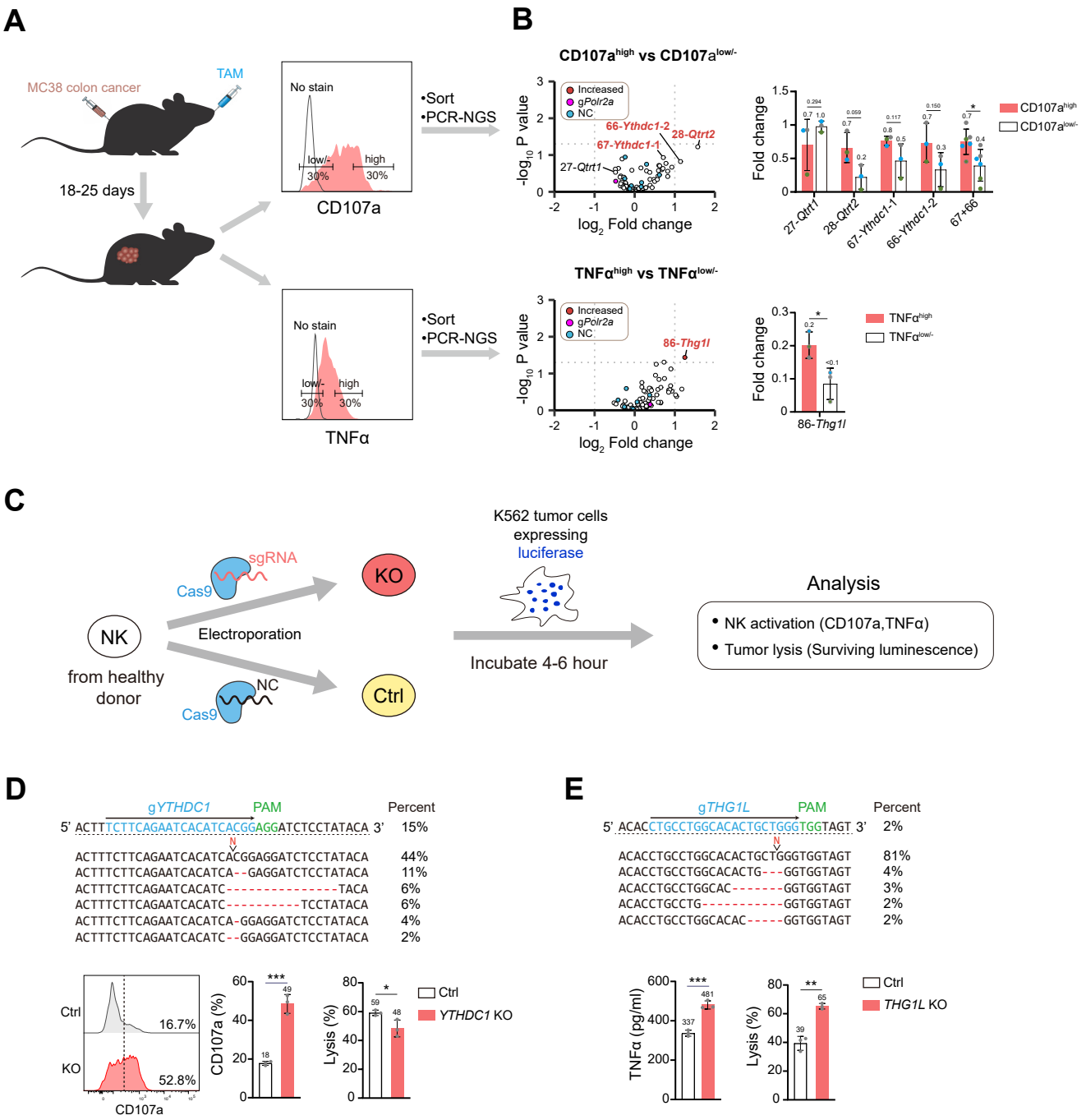

Figure 5. Screening and validation of NK regulators

(A-B) Genetic screens for NK regulators in tumor-bearing iMAP-91 mice. Tumor-infiltrating cells were stained for CD45.2, CD3 and NK1.1 together with CD107a (top plot) or intracellular TNFα (bottom plot) before indicated NK subsets were isolated by flow cytometry and analyzed by NGS. Source data in Table S3 (sheet 3).

(C) Workflow for target validation in human NK cells *in vitro*.

(D-E) Successful editing and its effects on NK function for *YTHDC1* (D) and *THG1L* (E). The data are from a single experiment, with a biological replicate shown in Figure S4D. *p < 0.05, **p < 0.01, ***p< 0.001, Student's t-test.

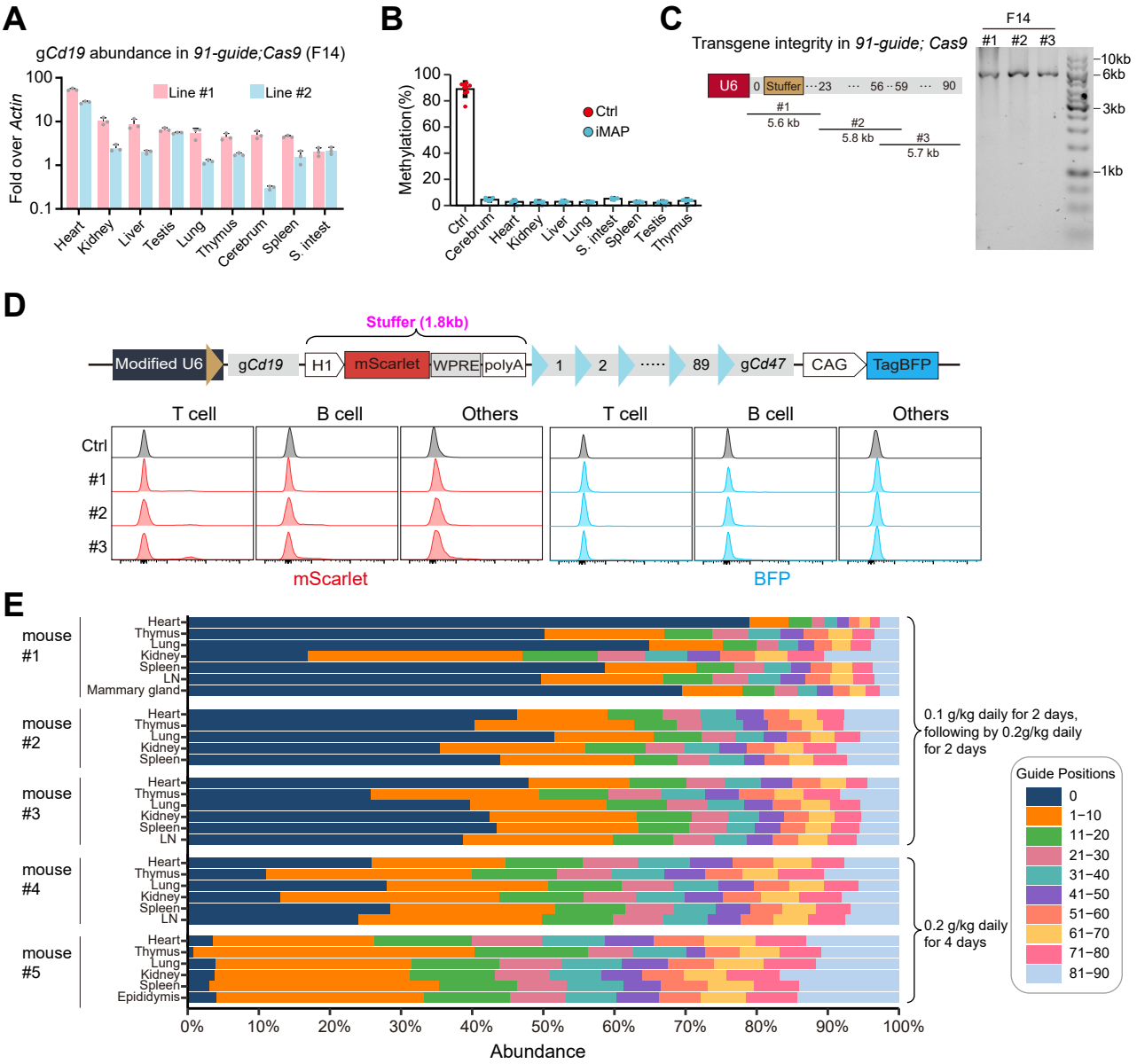

Figure S1. Basic features of the *91-guide* transgenic line, related to Figure 2

(A) qRT-PCR quantification of *gCd19* expression in two transgenic lines. Line #1 was selected for further experiments.

(B) Little U6 promoter CpG methylation at the U6 promoter. The *31-guide* transgene inserted into the H11 locus (red) serves as a positive control (Liu et al., 2022).

(C) PCR analysis of transgene integrity. The three overlapping amplicons are diagrammed. The mice were *91-guide; Cas9* of the F14 generation.

(D) FACS analysis showing mScarlet and BFP expression in peripheral blood cells. The two reporter proteins were expressed from the H1 promoter in the stuffer and the CAG promoter downstream of the *91-guide* transgene, respectively. Both promoters are driven by RNA Pol II, contrary to the RNA Pol III-dependent U6 promoter. Together with the fact that U6 promoter was active in this line (Figure S1A), the data reinforce the dichotomy in chromatin environment requirements for Pol II versus Pol III promoters (Liu et al., 2022).

(E) P0 guide composition of all the *91-guide; Cas9* samples, a subset of them used in Figure 2A (bottom). Source data in Table S2 (sheet 3).

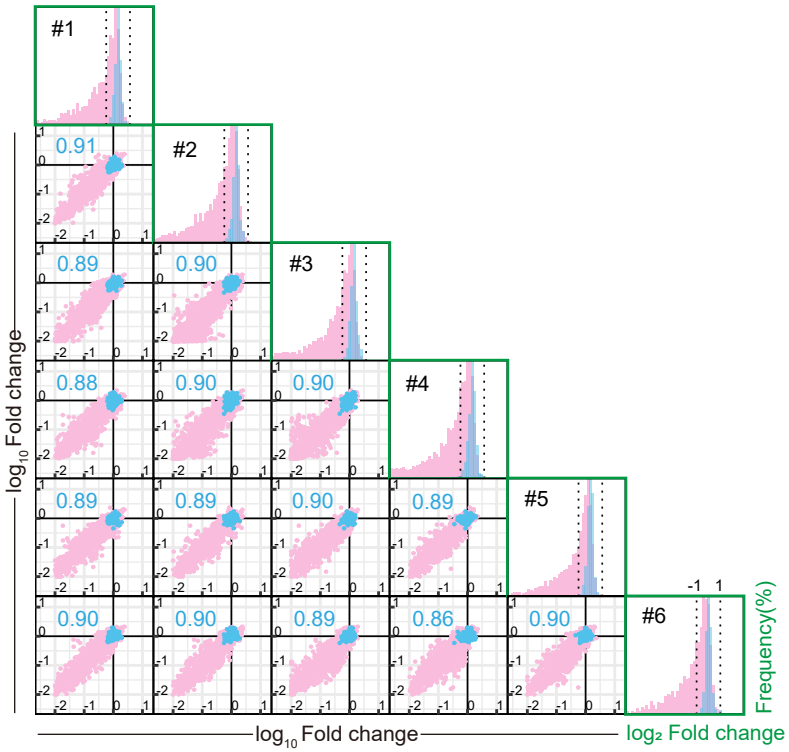

Figure S2. High replicate reproducibility of the NGS data in Figure 3
A total of 46 tissues, each with 2–6 (mostly 5-6) replicates, were sampled from six mice for profiling the targeting (pink) and NC (cyan) guides. The scatter plots and the histograms display pairwise comparisons and frequency distribution of the data points, respectively. Source data in Table S3 (sheet 1).

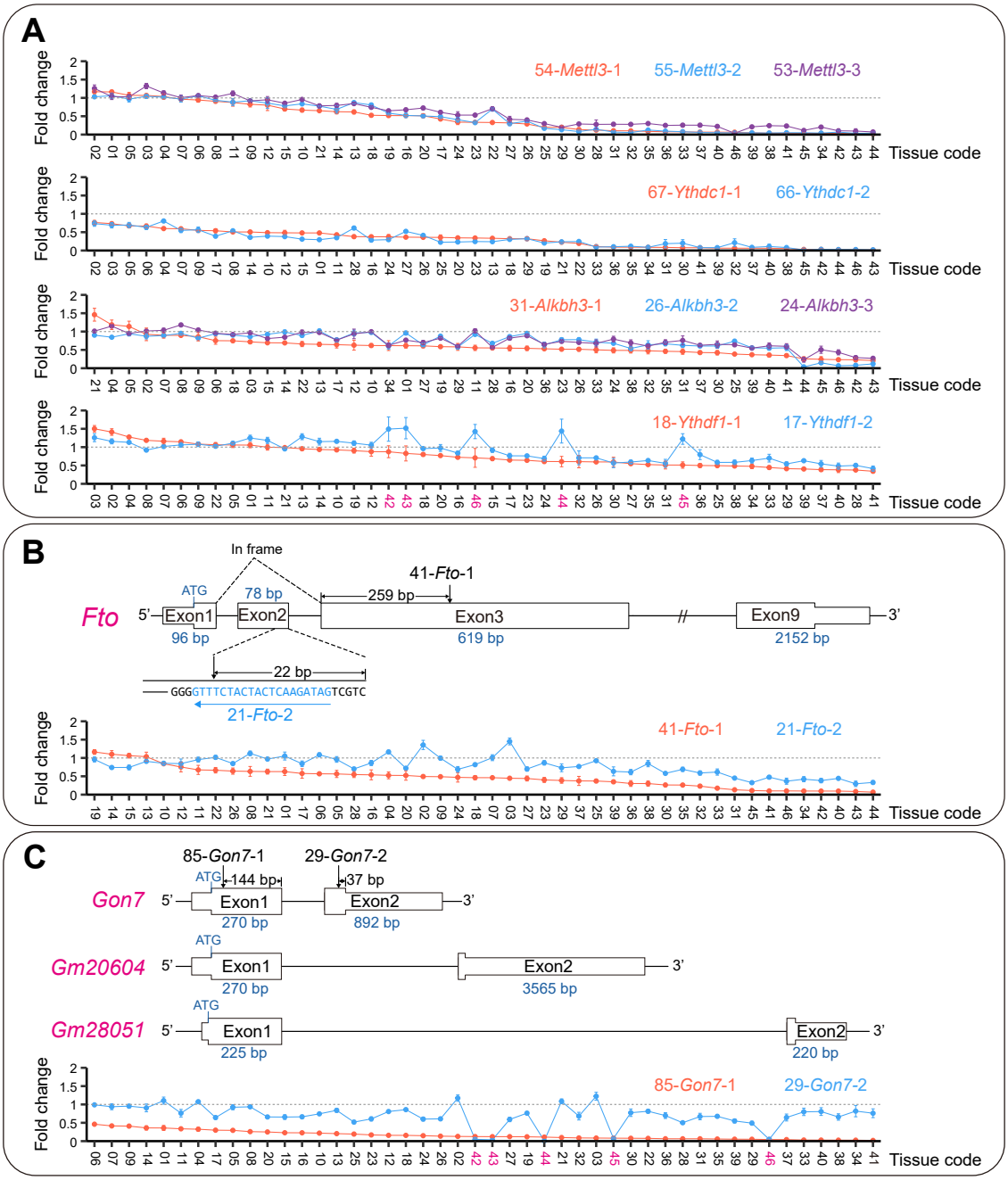

Figure S3. Analyzing different guides targeting the same genes, related to Figure 3D.
(A) Consistent depletion patterns of different guides designed to create null alleles of the same target genes. Of note, the two guides targeting *Ythdf1* (g17-18) closely co-segregated except that in the male germ cells (Tissue #42-46, pink), g17 (but not g16) was mildly enriched (<1.5x relative to NC). The discrepancy suggests off-target effects, reminiscent of the mild enrichment of g*Polr2a* in the testis in iMAP-61 line (Liu et al., 2022).
(B) Distinct depletion patterns of guides creating hypomorphic vs null *Fto* allele. FTO is 502-aa protein encoded by 9 exons. g41-*Fto*-1 is predicted to truncate FTO at ~aa128 to fully inactivate the protein, whereas g21-*Fto*-2 would likely cause Exon2-skipping by destroying its splicing donor, thus creating a partially active FTO mutant lacking the 26-aa fragment.
(C) Distinct depletion patterns of guides creating hypomorphic vs null *Gon7* allele. GON7 is 98-aa protein encoded by two exons, the first shared with two related genes (Gm20604, 28051). g85-*Gon7*-1 is predicted to fully inactivate *Gon7* together with the two related genes, whereas g29-*Gon7*-2 would likely create a partially active mutant lacking a~13-aa tail. g29-*Gon7*-2 was selectively depleted in male germ cells (Tissue #42-46, pink).

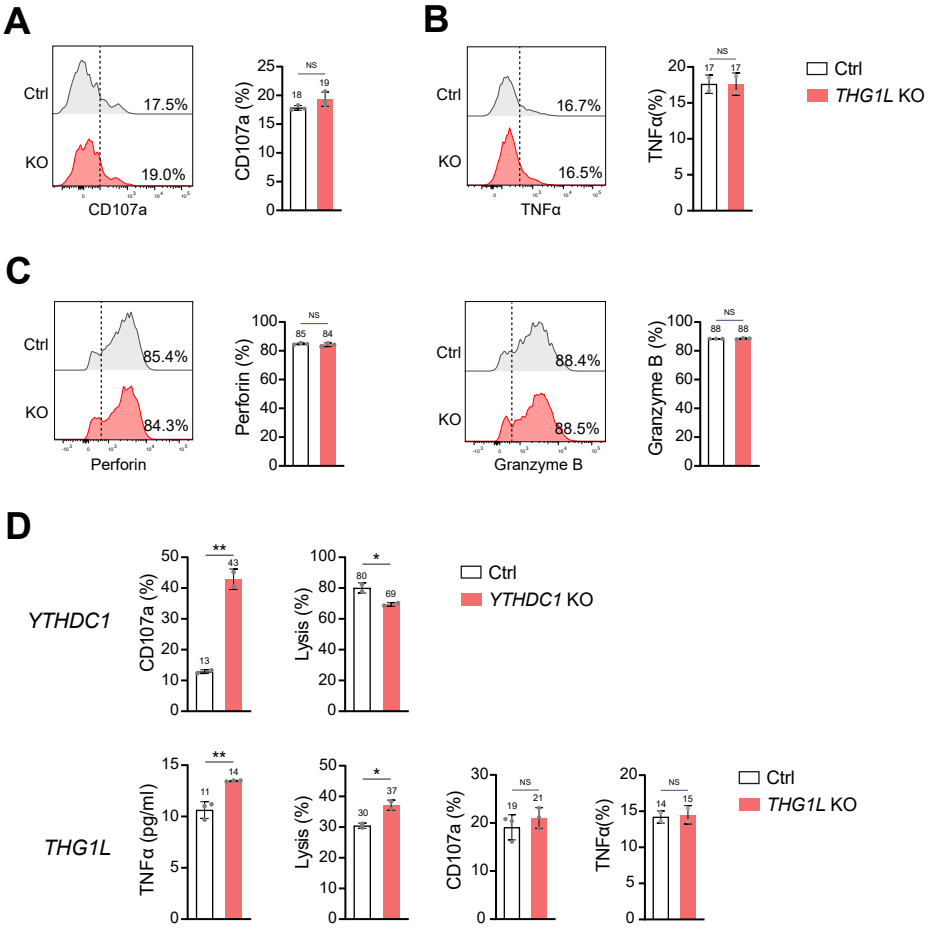

Figure S4. Target validation in human NK cells, related to Figure 5E
(A-C) Additional data from the experiment in Figure 5E.
(D) A biological replicate of the experiment in Figure 5D-E, showing the same trend.

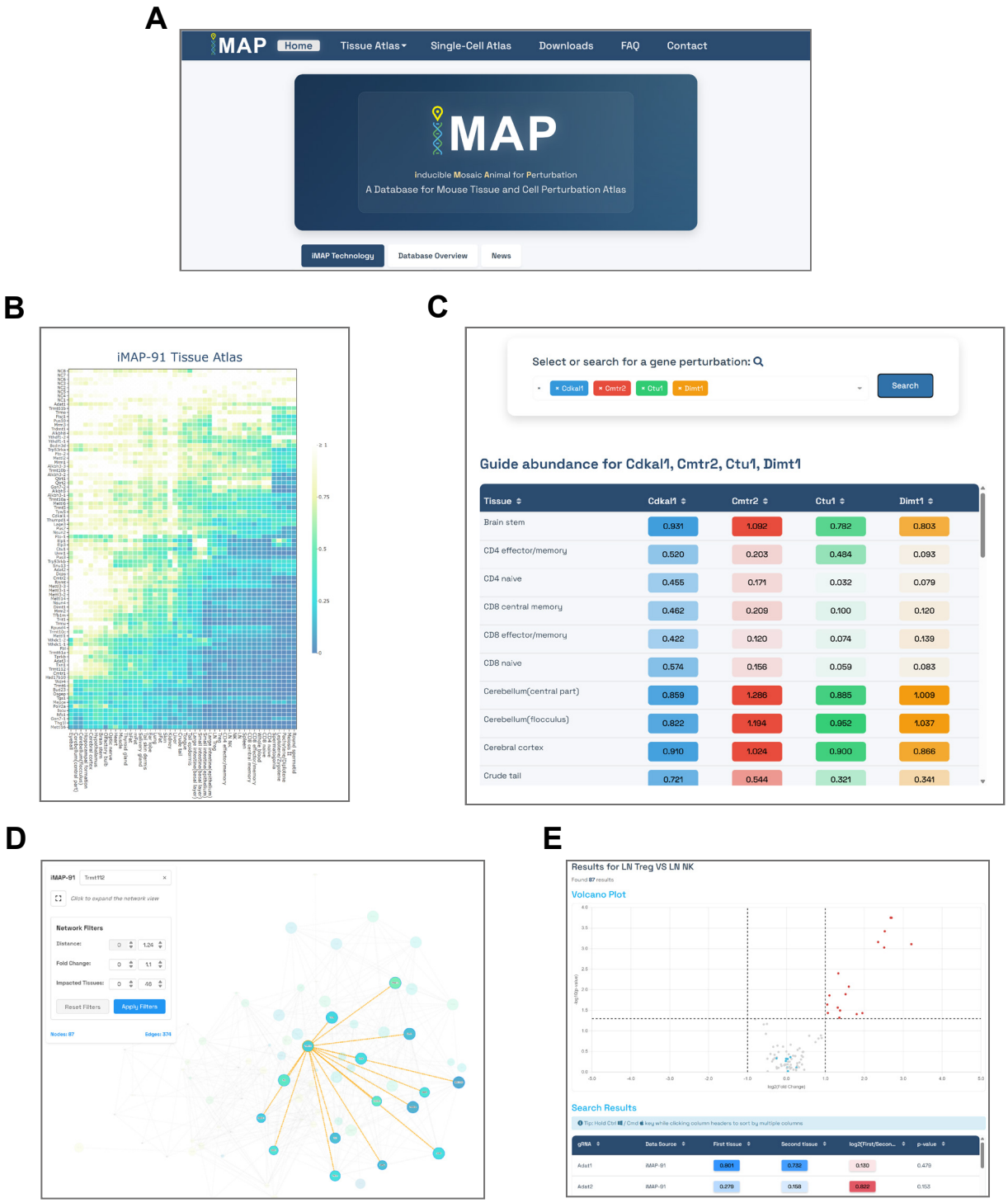

Figure S5. Snapshots of the iMAP database

(A) Home page.

(B) Heatmap view, displaying guide abundance across tissues. Actual fold-changes can be displayed by clicking on data points. One can also select a region of interest and zoom in.

(C) Search result for the abundance of guides of interest across diverse tissues.

(D) Search result for the network of guides surrounding a guide of interest. Each dot represents a guide. The color and size signify fold-change and the numbers of tissues affected, respectively. Additional information can be displayed by clicking on the guides and the lines connecting the guides.

(E) Search result for differentially represented guides between a pair of tissues.